Geochemistry, Geophysics, Geosystems

RESEARCH ARTICLE
10.1029/2018GC007900

Special Section:
Carbon degassing through volcanoes and active tectonic regions

Key Points:

- Sulfate sulfur and oxygen isotopes cofractionated during thermochemical sulfate reduction process
- The approximate length of TSR is 80 ka
- A combination of petrography, REE, fluid inclusion, and stable isotope measurements can be useful to disentangle the fluid history of a large CO_2 reservoir

Correspondence to:
C. Zwahlen,
zwahleca@gmail.com

Citation:
Zwahlen, C., Hollis, C., Lawson, M., Becker, S. P., Boyce, A., Zhou, Z., & Holland, G. (2019). Constraining the fluid history of a CO_2-H_2S reservoir: Insights from stable isotopes, REE, and fluid inclusion microthermometry. *Geochemistry, Geophysics, Geosystems*, *20*. https://doi.org/10.1029/2018GC007900

Received 13 AUG 2018
Accepted 18 DEC 2018
Accepted article online 19 DEC 2018

Constraining the Fluid History of a CO_2-H_2S Reservoir: Insights From Stable Isotopes, REE, and Fluid Inclusion Microthermometry

Carmen Zwahlen[1], **Cathy Hollis**[1], **Michael Lawson**[2], **Stephen P. Becker**[2], **Adrian Boyce**[3], **Zheng Zhou**[4], **and Greg Holland**[1]

[1]The University of Manchester, Manchester, UK, [2]ExxonMobil Upstream Research Company, Spring, TX, USA, [3]Scottish Universities Environmental Research Centre (SUERC), East Kilbride, UK, [4]Lancaster Environment Centre, Lancaster University, Lancaster, UK

Abstract Reservoirs that host CO_2-H_2S-bearing gases provide a key insight into crustal redox reactions such as thermochemical sulfate reduction (TSR). Despite this, there remains a poor understanding of the extent, duration, and the factors limiting this process on a reservoir scale. Here we show how a combination of petrography, fluid inclusion, rare earth element (REE), and carbon ($\delta^{13}C$), oxygen ($\delta^{18}O$), and sulfur ($\delta^{34}S$) stable isotope data can disentangle the fluid history of the world's largest CO_2 accumulation, the LaBarge Field in Wyoming, USA. The carbonate-hosted LaBarge Field was charged with oil around 80 Ma ago, which together with nodular anhydrite represent the reactants for TSR. The nodules exhibit two distinct trends of evolution in $\delta^{13}C$ with both $\delta^{34}S$ and $\delta^{18}O$ that may be coupled to two different processes. The first trend was interpreted to reflect the coupled dissolution of anhydrite and reduction to elemental sulfur and the oxidation of organic compounds and associated precipitation of calcite during TSR. In contrast, the second trend was interpreted to be the result of the hydrothermal CO_2 influx after the cessation of TSR. In addition, mass balance calculations were performed to estimate an approximate TSR reaction duration of 80 ka and to identify the availability of organic compounds as the limiting factor of the TSR process. Such an approach provides a tool for the prediction of TSR occurrence elsewhere and advancing our understanding of crustal fluid interactions.

1. Introduction

Study of fluid-fluid and fluid-rock interactions in gas reservoirs containing elevated concentrations of CO_2-H_2S assists not only in understanding processes that control migration and accumulation of crustal fluids but also the feasibility of CO_2-H_2S cosequestration (Glezakou et al., 2012; Kaszuba et al., 2011; Knauss et al., 2005; Pearce et al., 2016; Williams & Paulo, 2002; Xiao et al., 2009; Zhang et al., 2011). In addition, the formation of H_2S in natural gas reservoirs is of interest for drilling security and the estimation of gas degradation and presence of mineral deposits (e.g., Mississippi Valley-type deposits; Piqué et al., 2009; Powell & MacQueen, 1984). However, sulfur cycling and redox reactions such as thermochemical sulfate reduction (TSR) are not well understood on a reservoir scale and only a few natural systems have been studied including the Khuff Formation, Saudi Arabia (Bildstein et al., 2001; Jenden et al., 2015; Worden et al., 1995, 2000; Worden & Smalgeoley, 1996), the Smackover Formation, USA (Claypool & Mancini, 1989; Heydari & Moore, 1989), Lower Saxony Basin, Germany (Biehl et al., 2016), Tarim and Sichuan Basin, China (Cai et al., 2001, 2003, 2004, 2009, 2010, 2013, 2016; Hao et al., 2015; Jiang et al., 2014, 2015, Liu et al., 2013, 2014), and the Nisku Formation, Canada (Machel, 1987a, 1987b, 2001; Riciputi et al., 1994). Since the reactions are difficult to simulate experimentally under reservoir conditions, due to their slow rates of reaction (Amrani et al., 2008; Anderson & Thom, 2008; Ding et al., 2008, 2009, Yue et al., 2005, 2006), natural CO_2-H_2S reservoirs form ideal natural analogues for CO_2-H_2S cosequestration (Allis et al., 2001; Bickle et al., 2013; Kaszuba et al., 2011).

The LaBarge Field located in western Wyoming, USA, hosts an estimated 4.7×10^{12} m^3 (167 trillion cubic feet) of gas (Stilwell, 1989), of which 66% is CO_2, in the Mississippian-aged Madison Formation (Figure 1). While the mineralogy, petrography, and sequence stratigraphy of the Madison Formation in Wyoming have been studied comprehensively in the past (Budai, 1985; Budai et al., 1984; Budai & Cummings, 1987; Buoniconti, 2008; Katz, 2008; Katz et al., 2007; Smith et al., 2004; Sonnenfeld, 1996b), there is a relative

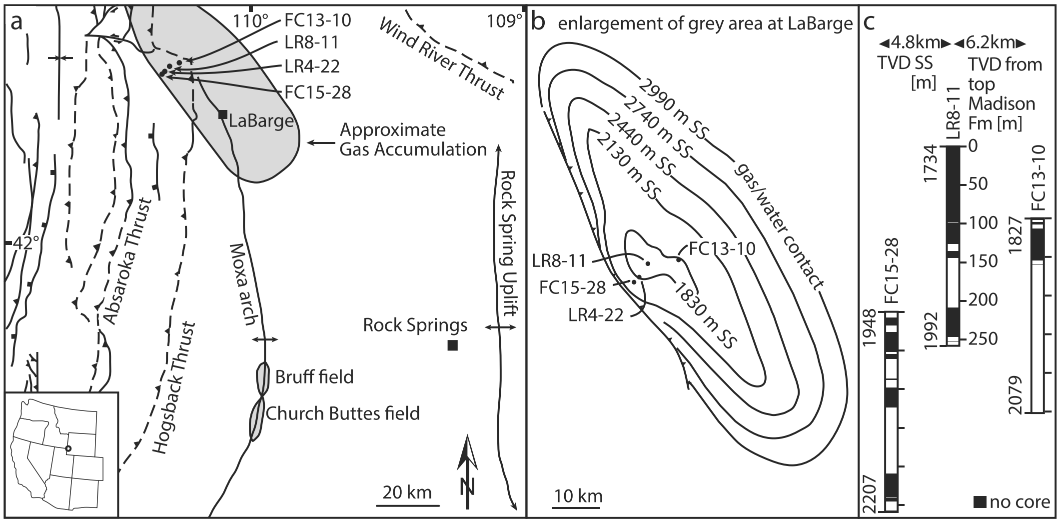

Figure 1. (a) Map of the Moxa Arch with main tectonic features in the area modified after Becker and Lynds (2012). The LaBarge Field is colored in gray. (b) Map of the LaBarge Field with contour lines of the top of the Madison Formation and gas water contact in TVD SS modified after Stilwell (1989). (c) Integrity of three viewed drill cores and their relative depth in the Moxa Arch.

paucity of petrographic observations from the LaBarge Field. The gas forms a 250-m-thick gas column and is the largest known natural CO_2 accumulation in the world (Allis et al., 2001; Lynds et al., 2010; Stilwell, 1989). Different sources for the CO_2 and H_2S at the LaBarge Field have been proposed including thermal degradation of hydrocarbons, breakdown of carbonates, volcanic gas migration, and TSR (De Bruin, 2001; Huang et al., 2007; Stilwell, 1989). TSR is a redox reaction where sulfate is reduced to form hydrogen sulfide and hydrocarbons are simultaneously oxidized to form carbon dioxide (Orr, 1974). The volume of CO_2 in the LaBarge Field exceeds the volume of H_2S by a factor >12, which makes TSR a single source for CO_2, unlikely given that TSR produces CO_2 and H_2S in a molar ratio less than 1:1 (Liu et al., 2013). Despite these numerous studies, it has so far been difficult to unambiguously determine the origin of these non hydrocarbon gases in the field.

This paper provides new insights into the timing, extent, and duration of TSR at the LaBarge Field, which are crucial to improve the general understanding of TSR. The mineralogy and petrography of three drill cores from the Madison Formation will be presented as a precursor to a detailed geochemical characterization of different mineral phases in this formation. The geochemical assessment integrates rare earth element (REE), stable isotope, and fluid inclusion analysis to provide new constraints on the sulfate source and the onset of TSR. It will be discussed how this information can be used to estimate the duration of TSR at the LaBarge Field and elucidate the limiting factors during this process. The insights developed by this study may be used to better understand TSR, fluid-fluid, and fluid-rock interactions in other systems that have experienced multiple contributions of exogenously sourced fluid.

2. Tectonic and Geological Setting and Burial History

The LaBarge field is located at the north end of the Moxa Arch structure in Wyoming (USA), which is part of the Greater Green River Basin (Figure 1). On the west side, the LaBarge Field is confined by an eastward plunging basement involved reverse fault (Dixon, 1982; Kraig et al., 1987; Stilwell, 1989; Figure 1b). The gas trapped in the LaBarge Field consists on average of 66% CO_2, 21% CH_4, 7% N_2, 5% H_2S, and 0.6% He (Huang et al., 2007). The Madison Formation consists of alternating limestone and dolomite (Huang et al., 2007) and exhibits an average porosity of 8%–10%, a permeability of 10–50 mD, and a residual water saturation of 10% (Huang et al., 2007). The limestone and dolomite beds reach maximum thicknesses of 20 m with dolomite slightly dominating in abundance over limestone. Except for microinclusions, there is no primary anhydrite left; however, intercalated nodular calcite has been interpreted to represent a replacement of a former anhydrite phase (King et al., 2014; Thayer, 1983). These nodules occur in layers or as single

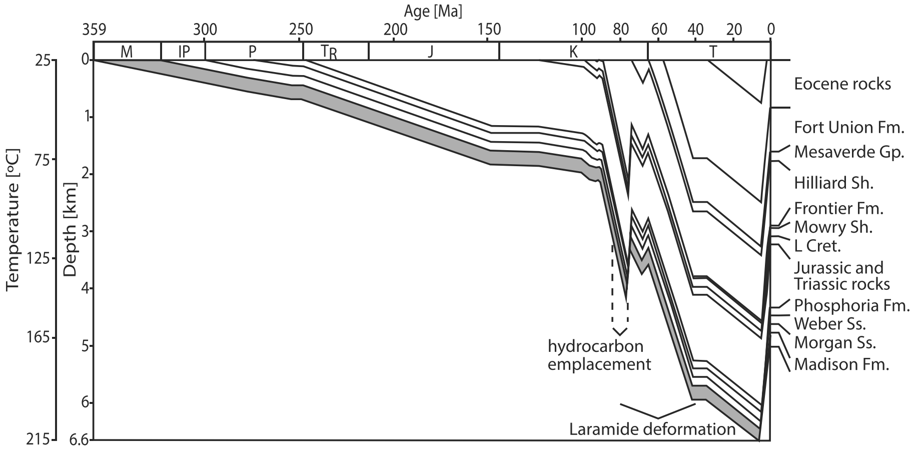

Figure 2. Burial history modified after Roberts et al. (2005) and adapted to 500 m further uplift at the LaBarge Field in the last 5 Ma. The Madison Formation is highlighted in gray. Fm., formation; Sh.,shale; Gp., group; Ss., sandstone; L. Cret., Lower Cretaceous rocks. The surface temperature has been set at 25 °C.

nodules throughout the formation with a slight increase toward the bottom of the formation but make up only around 0.2% of the total rock volume. Additional former evaporite beds are reported to have been dissolved, as evidenced by the presence of solution collapse breccias, but the volume of these features is more difficult to quantify (Budai & Cummings, 1987; Katz et al., 2006; Middleton, 1961; A. E. Roberts, 1966; Smith et al., 2004; Thayer, 1983).

The Moxa Arch is an anticline with a north-south oriented hinge line that borders the Wyoming fold and thrust belt to the west and the Rock Springs Uplift to the east. The anticline formed during the thick-skinned Laramide deformation from the Campanian until the Eocene (Becker & Lynds, 2012; Campbell-Stone et al., 2011; Kraig et al., 1987). At the same time, the thin-skinned Sevier fold and thrust belt migrated east toward the Moxa Arch (Blackstone, 1979; Dixon, 1982; Kraig et al., 1987; Nozaki et al., 1997; Wach, 1977). The most eastern thrust sheet, the Hogsback thrust, overruns the Moxa Arch at the LaBarge Field and displaces the sedimentary section that predates the Triassic (Becker & Lynds, 2012; Kraig et al., 1987). In the Late Cretaceous (84–76 Ma) Laramide-related burial drove the Permian Phosphoria Formation to depths sufficient for oil and gas generation. These fluids migrated down into the Madison Formation due to overpressure during maturation (Johnson, 2005; Figure 2). The Pennsylvanian Weber Sandstone Formation overlying the Madison Formation acted as a carrier bed during oil migration, but its permeability decreased over time due to cement precipitation until it formed a good seal for fluids hosted in the Madison Formation (Johnson, 2005). A burial history for the Moxa arch region has been established at the Bruff field, 30 km south of LaBarge (Roberts et al., 2005). The burial history is characterized by variable sedimentation rates and erosional events at 92, 75, 66, and 5 Ma until today (Roberts et al., 2005). The burial history of the LaBarge Field differs from the Bruff field by an additional 500 m of structural relief in Pliocene times. Maximum burial was reached at 5 Ma with a maximum burial temperature of approximately 215 °C (Roberts et al., 2005), whereas the present-day temperature of the Madison Formation is approximately 135 °C.

3. Samples and Method

3.1. Samples

Host rock limestone, dolomite, pyrite and calcite veins, and nodules were sampled from three cores of the Madison Formation from the LaBarge field, located on the crest of the Moxa Arch or slightly off crest (Figures 1 and 3). In total, 20 samples were collected from drill core FC13-10, 12 samples from drill core FC15-28, and 7 samples from drill core LR8-11 (Figures 1 and 3 and Table 1). Drill core LR4-22 was not viewed, but one sample of this drill core was available for analysis. The calcite veins and nodules were selected to represent different depths and nodule abundances of the drill cores. Pyrite was mainly found in drill cores FC15-28 and FC13-10, whereas LR8-11 only contained one location suitable for pyrite

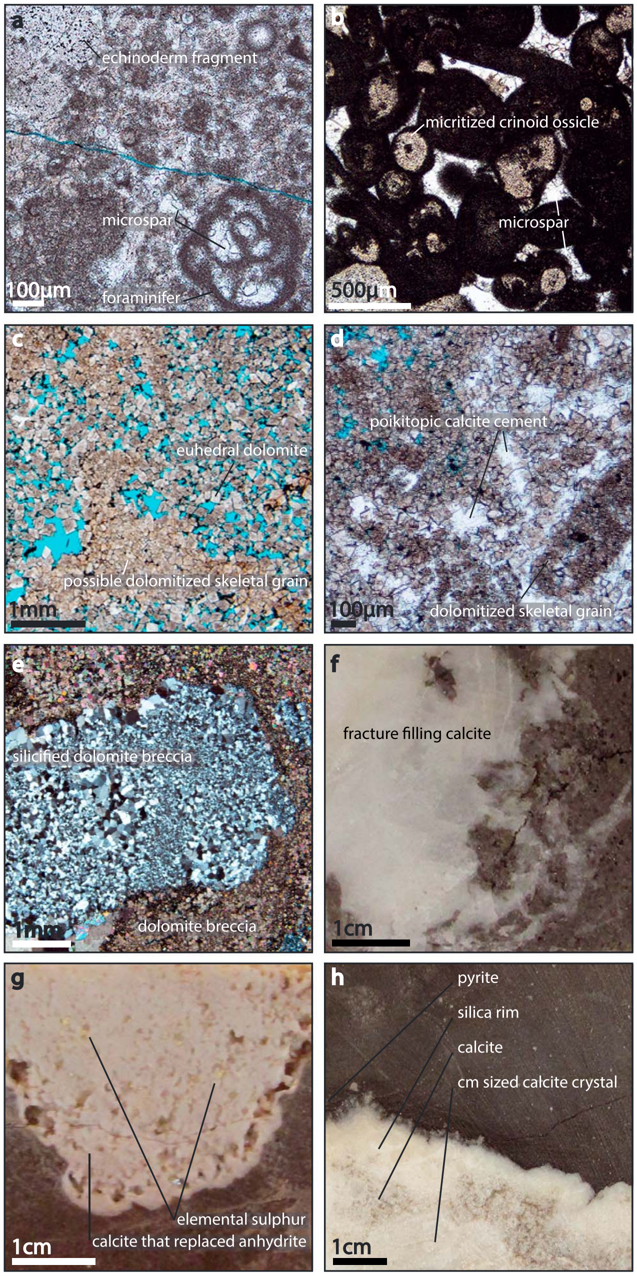

Figure 3. (a and b) Madison limestone consisting of partially micritized foraminifers, brachiopods, bivalve, and echinoderm fragments with microspar filling the pore space; (c) fabric-preserving euhedral to subhedral dolomite with high intercrystalline porosity; (d) fabric-preserving euhedral to subhedral dolomite with poikilotopic calcite cement filling the pore space; (e) partially silicified dolomite breccia; (f) fracture-filling calcite in dolomite host rock (sample C6); (g) former anhydrite nodule replaced by calcite with elemental sulfur precipitated in between calcite crystals (sample S2); and (h) former anhydrite nodule replaced by a succession of chalcedony and quartz precipitated in the rim, followed by 100–500-µm-sized calcite crystals (sample A1(F)) and a centimeter-sized calcite crystal in the center (sample A1(C)).

sampling. Additionally, two native sulfur samples were collected from drill cores FC15-28 and FC13-10. All samples were fist size pieces of drill core, which were then cut for thin sections. Minerals were identified visually by a Nikon Eclipse LV100NPOL microscope and analytically by a JEOL 6400 scanning electron microscope at the University of Manchester. The samples were then cut into smaller pieces of interest and crushed for further analytical measurements. The abundance of anhydrite for TSR has been estimated from calcite that replaced former anhydrite nodules through drill core logging, and the amount of pyrite has also been estimated from drill core logging.

3.2. Stable Isotopes

Carbon (δ^{13}C) and oxygen (δ^{18}O) isotope measurements were performed on 32 calcite and dolomite samples on an Isoprime multiflow mass spectrometer at Lancaster University (Table 1). Dolomite samples were first added to 1-M HCl for 1 hr and rinsed with deionized water to remove any traces of calcite (De Groot, 2009). Following this, 400 µg of sample powder was added to phosphoric acid to evolve CO_2, which was subsequently analyzed. All data were corrected to PDB (Pee Dee Belemnite) using international standards LSVEC (δ^{13}C −46.6‰, δ^{18}O −26.7‰), NBS-18 (δ^{13}C −5.014‰, δ^{18}O −23.2‰), and CO1 (δ^{13}C +2.492‰, δ^{18}O −2.4‰). Precision for five standard replicates ($n = 5$, 1 standard deviation [SD]) was <0.1‰ for carbon and oxygen isotopes.

Additionally, 17 calcite nodules were analyzed for sulfur (δ^{34}S) and oxygen (δ^{18}O) isotopes in carbonate associated sulfate (CAS; Table 1. A total of 900 mg of crushed sample was dissolved and reprecipitated as $BaSO_4$ following the filtration method of Wynn et al. (2008). Two samples (C7 and A3) did not yield the minimum of 250 and 350 µg of $BaSO_4$ for the sulfur and oxygen isotope analyses, respectively. One sample (C9) gave enough $BaSO_4$ for sulfur isotope analysis but not for oxygen isotope analysis. The isotopic ratios were determined by continuous flow isotope ratio mass spectrometry using the Isoprime 100 mass spectrometer linked to an Elementar Pyrocube analyzer at the University of Lancaster (Wynn et al., 2014). Sulfur and oxygen isotopic data are presented relative to V-CDT (Vienna-Canyon Diablo Troilite) and V-SMOW (Vienna-Standard Mean Ocean Water), respectively. The international standards NBS-127 (+21.1‰) and SO_5 (+0.5‰) were used to calibrate sulfur isotope data. For the oxygen isotopes the international standards NBS-127 (+9.3‰) and SO_6 (−11.35‰) were used. The precision for standard replicates ($n = 4$, 1SD) was <0.1‰ for sulfur and <0.2‰ for oxygen. Three samples (C4, C5, and C11) contained pyrite grains, which oxidized during the preparation procedure and lead to contamination (Marenco et al., 2008) and were therefore excluded.

Oxygen isotopes were analyzed on three quartz samples on a Finnigan MAT 253 mass spectrometer at the British Geological Survey following the fluorination method described by Clayton and Mayeda (1963; Table 1). The samples were added to 1-M HCl and rinsed with deionized water prior to analysis in order to remove any calcite from the samples. The data are corrected to V-SMOW using the standard BFC (M. Leng et al., 2001; M. J. Leng & Sloane, 2008; assumed value 29‰). The precision for standard replicates was <0.1‰, and the sample reproducibility (1SD) was 0.1‰.

Pyrite sulfur isotope measurements were carried out at Scottish Universities Environmental Research Centre (Table 1). The pyrite samples were converted to SO_2 by combustion under vacuum at 1070 °C with cuprous oxide after the method of Robinson and Kusakabe (1975). The gas was then purified cryogenically and analyzed on a VG SIRA II gas mass spectrometer. The two native sulfur samples were measured in the same way as the pyrites. The sulfur isotopic data were corrected to V-CDT using the international standards NBS-123 (+17.1‰), International Atomic Energy Agency-S-3 (−31‰), and the internal lab standard CP-1 (−4.6‰).

3.3. Rare Earth Elements

Rare earth element concentrations in 15 calcite nodules were measured on an Agilent 7500cx ICP-MS at the University of Manchester (Table 1 and 2 and Figure 4). The 100 mg of crushed calcite sample was digested overnight in 5 ml of 6-M HCl. A subsample of the liquid phase was extracted and diluted to a <0.1% total dissolved solids (TDS) solution for analysis. Typical relative errors for REE standard concentrations were less than 5%. The concentrations were normalized to Post-Archean Average Australian Shale (McLennan, 1989; Nance & Taylor, 1976). Two samples (C1 and A3) exhibit very low REE concentrations (on the same level as the measured blanks) and are therefore excluded from the following interpretation. In three samples (A2, C14, and C10) the Ho concentration is below the blank level and was also excluded from this interpretation. In eight samples the europium concentration was corrupted by barium oxide interference (Dulski, 1994; Jarvis et al., 1989; Figure 4b). In these samples the Ba concentration is up to 2,200 ppm and shows an almost perfect linear correlation with the Eu concentration ($R^2 = 0.98$; Figure 4e). The remaining five samples (C4, C5, C6, C11, and& C12) lie above this trend with a low Ba concentration and are considered reliable.

3.4. Fluid Inclusions Microthermometry

Fluid inclusion homogenization temperatures were measured on double-polished thin sections at ExxonMobil Upstream Research Company (Texas, USA) and Fluid, Inc. (Colorado, USA; Table 3). The fluid inclusion analyses were conducted on different samples than the REE and stable isotope measurements except for sample Q2. Fluid inclusion analysis was performed following the fluid inclusion assembly method described by Goldstein and Reynolds (1994) and reported as the range of homogenization temperatures found in the assemblage with the number of inclusions observed (Table 3). This technique consists of finding the highest homogenization temperature (Th) for aqueous, methane-bearing, fluid-inclusion assemblages. The temperature at which the fluid inclusion was trapped is recorded in the homogenization temperatures of aqueous fluid inclusions. Fluid inclusions examined in this study occur as both primary and secondary inclusions in different mineral phases (dolomite, quartz, fracture-filling calcite, fluorite, and calcite that replaced anhydrite). Because gas inclusions are present in all observed phases coexisting with many of these aqueous inclusion assemblages, the assumption is that no pressure correction is required, and thus, the T_h value represents a true original trapping temperature along the water liquid-vapor saturation (or bubble point) curve. Thus, primary inclusions represent an original crystallization temperature of the mineral growth zone in which they are hosted, and secondary inclusions potentially represent a maximum temperature postcrystallization. The homogenization temperatures of aqueous fluid inclusions can provide accurate estimates of maximum temperature at peak burial or record the process of some anomalous temperatures not related to burial, such as hydrothermal activity.

4. Results

4.1. Mineralogy and Petrography

The Madison Formation in the LaBarge Field is dominated by skeletal packstone (Figures 3a and 3b). The bioclasts are 50–300 μm in size and include foraminifers and brachiopods, bivalve, and echinoderm fragments. All skeletal grains are micritized except for some echinoderm fragments (Figures 3a and 3b). All primary interparticle and intraparticle porosity is cemented by microspar. Based on the viewed drill cores, approximately 60% of the Madison Formation limestone is pervasively dolomitized (Figure 3c). The dolomite is finely crystalline and equigranular with a crystal size of approximately 50 μm. The crystal shapes are euhedral, whereas some micritized skeletal grains are replaced by subhedral dolomite (Figure 3c). The dolomite is fabric preserving and can have high intercrystalline porosity. Part of this porosity is subsequently filled with

Table 1
Rare Earth Element and Yttrium Concentrations and Their Relative Standard Error

Drill core	Sample ID	Mineral phase	Distance to top Madison [m]	TVD SS (m)	Carbonate $\delta^{13}C$V-PDB (‰)	Carbonate $\delta^{18}O$V-PDB (‰)	Pyrite/sulfur $\delta^{34}S$V-CDT (‰)	CAS $\delta^{34}S$V-CDT (‰)	CAS $\delta^{18}O$V-SMOW (‰)	Quartz $\delta^{18}O$V-SMOW (‰)	REE measurement
FC13-10	S1	Elemental sulfur	3.4	1830.4			−0.2				
FC13-10	P4	Pyrite	249.6	2076.6			−30.2				
FC13-10	P5(1)	Pyrite	250.3	2077.3			−33.2				
FC13-10	P5(2)	Pyrite	250.3	2077.3			−20.5				
FC13-10	P1	Pyrite	8.4	1835.4			6.6				
FC13-10	P2	Pyrite	203.9	2030.9			8.8				
FC13-10	P3	Pyrite	210.5	2037.5			9.5				
FC13-10	A1(C)	Calcite that replaced anhydrite (core)	245.8	2072.8	−11.0	−11.8		22.0	18.6		yes
FC13-10	A1(F)	Calcite that replaced anhydrite (rim)	245.8	2072.8	−9.9	−12.2		18.4	17.6		yes
FC13-10	A2	Calcite that replaced anhydrite	253.6	2080.6	−8.6	−12.9		18.8	15.9		yes
FC13-10	C12	Fracture-filling Calcite	107.3	1934.3	1.2	−6.8		15.3	14.7		yes
FC13-10	C13	Calcite that replaced anhydrite	176.1	2003.1	−15.2	−13.7		20.5	17.6		
FC13-10	C7	Calcite that replaced anhydrite	241.4	2068.4	−9.2	−12.5		x	x		
FC13-10	C7(L)	Limestone	241.4	2068.4	1.8	−8.9					
FC13-10	A3	Calcite that replaced anhydrite	242.2	2069.2	−5.9	−13.6		x	x		x
FC13-10	D1	Dolomite	169.8	1996.8	3.3	−3.3					
FC13-10	D2	Dolomite	82.0	1909.0	1.9	−2.9					
FC13-10	D3	Dolomite	147.3	1974.3	2.9	−2.2					
FC13-10	D4	Dolomite	213.3	2040.3	7.2	0.0					
FC13-10	L1(1)	Limestone	157.6	1984.6	1.5	−8.2					
FC13-10	L1(2)	Limestone	157.6	1984.6	1.7	−7.3					
FC13-10	A4(D)	Saddle dolomite	230.6	2057.6	1.9	−9.8					
FC13-10	A4	Fracture-filling calcite	230.6	2057.6	1.0	−9.4					
FC13-10	A4(L)	Limestone	230.6	2057.6	2.9	−7.3					
FC13-10	Q1	Quartz	175.0	2002.0						27.5	
FC13-10	Q2	Calcite that replaced anhydrite and quartz	12.6	1839.6	−18.3	−12.2				28.1	
FC15-28	S2	Calcite that replaced anhydrite/ elemental sulfur	205.2	2153.2	−8.2	−13.3	10.7				
FC15-28	P6	Pyrite	205.7	2153.7			8.0				
FC15-28	P7	Pyrite	209.0	2157.0			6.6				
FC15-28	P8	Pyrite	249.4	2197.4			4.1				
FC15-28	P9	Pyrite	255.0	2203.0			7.9				
FC15-28	P10	Pyrite	257.0	2205.0			3.6				
FC15-28	C10	Calcite that replaced anhydrite	62.3	2010.3	−8.2	−13.6		15.3	15.1		yes
FC15-28	C5	Calcite that replaced anhydrite	255.0	2203.0	−13.9	−10.0		x	x		yes
FC15-28	C4	Calcite that replaced anhydrite	255.1	2203.1	−9.8	−9.7		x	x		yes

Table 1 *(continued)*

Drill core	Sample ID	Mineral phase	Distance to top Madison [m]	TVD SS (m)	Carbonate δ^{13}CV-PDB (‰)	Carbonate δ^{18}OV-PDB (‰)	Pyrite/sulfur δ^{34}SV-CDT (‰)	CAS δ^{34}SV-CDT (‰)	CAS δ^{18}OV-SMOW (‰)	Quartz δ^{18}OV-SMOW (‰)	REE measurement
FC15-28	C11	Calcite that replaced anhydrite	206.3	2154.3	−10.3	−10.9		x	x		yes
FC15-28	A5	Fracture-filling calcite	172.8	2120.8	2.3	−6.6					
FC15-28	C6	Fracture-filling calcite	135.3	2083.3	0.7	−10.0					yes
LR4-22	LB2	Fracture-filling calcite	136.9	1920.0	1.7	−9.3					
LR8-11	P11	Pyrite	256.9	1990.9			−19.5				
LR8-11	C1	Calcite that replaced anhydrite	254.8	1988.8	−16.6	−9.6		21.6	17.8		x
LR8-11	C14	Calcite that replaced anhydrite	249.3	1983.3	−12.3	−9.1		21.3	17.7		yes
LR8-11	C2	Calcite that replaced anhydrite	206.3	1940.3	−14.8	−11.1		22.7	17.9		yes
LR8-11	C3	Calcite that replaced anhydrite and quartz	251.0	1985.0	−13.5	−8.6		22.3	18.2	28.1	
LR8-11	C8	Calcite that replaced anhydrite	172.9	1906.9	−9.3	−11.4		18.8	17.2		yes
LR8-11	C9	Calcite that replaced anhydrite	152.8	1886.8	−13.7	−12.5		20.9	x		yes

poikilotopic calcite cement with crystal sizes up to 3 mm (Figure 3d). Bedding parallel low- (0.5 cm) and high (3 cm)-amplitude stylolites are found mainly in the limestone but occur also in the dolomite.

In addition to limestone and dolomite, silicified limestone occurs in three different forms: bedding parallel bands of silicified limestone, chalcedony, and quartz along the rim of former anhydrite nodules and silicified dolomite breccia. The silicified limestone bands are bound by stylolites and consist mainly of 20- to 100-μm anhedral quartz crystals. These crystals are precipitated around and partially replacing skeletal grains. They are mainly found in drill cores FC15-28 and LR8-11 around 140 and 250 m beneath the top of the Madison Formation. The second silica form consists of chalcedony rosettes 1 mm in diameter and submilimeter, anhedral, and sometimes radially oriented quartz crystals. The chalcedony and quartz crystals are precipitated in the rims of former anhydrite nodules and in one case replaced the former anhydrite nodule completely (Figure 3h). This silica form encompasses significant volumes of anhydrite and some fluorite inclusions and is most abundant in drill core FC13-10. The third silica form is a silicified dolomite breccia composed of in-equigranular concretion of <200-μm-sized anhedral quartz crystals surrounded by equigranular 10-μm-sized anhedral quartz crystals (Figure 3e). The coarser quartz crystals sometimes form pseudomorphs of quartz after dolomite. The dolomite around the quartz forms concretions of coarser dolomite surrounded by very fine grained dolomite. This suggests that the quartz is not brecciated itself but replaced and cemented a dolomite breccia. The dolomite breccia replacing quartz occurs in all three drill cores at 2,123-, 1,913-, and 2,001-m true vertical depth subsea (TVD SS) in drill cores FC15-28, LR8-11, and FC13-10, respectively. These depths correspond to approximately 176m depth from the top of the Madison Formation in all three drill cores.

Besides the microspar, there are two more forms of authigenic calcite: fracture-filling calcite and calcite that replaced anhydrite. The fracture-filling calcite forms subhedral blocky calcite crystals up to several centimeters in diameter that are precipitated in fractures in the limestone and dolomite host rock (Figure 3f). Sparse pyrite, galena, and apatite microinclusions and quartz and fluorite crystals are enclosed by this calcite phase. This phase is abundant in drill cores FC15-28 and FC13-10 but has not been found in drill core LR8-11.

Fluorite is found in two different forms at two different times in the paragenetic sequence: the first occurrence is as inclusions in quartz, fracture-filling calcite, and calcite that replaced anhydrite and the second occurrence is as fracture-filling fluorite. The inclusions are up to 15 μm in size and sometimes associated with anhydrite inclusions. The fluorite-cemented fracture consists of 1-mm-sized anhedral crystals and crosscuts and fills a reopened calcite-cemented fracture in drill core FC15-28 at 2,120.1-m TVD SS. Subhedral saddle dolomite crystals, 5 mm in size, are found in drill core FC13-10 at 2,057-m TVD SS. The saddle dolomite encloses quartz, fluorite, and fracture-filling calcite crystals.

The former anhydrite nodules are completely replaced by calcite except for some microinclusions (Figures 3g and 3h and Appendix A). This calcite phase exhibits anhedral to subhedral crystals from 100 to 500 μm in size with an interlocking fabric. Two calcite nodules have a centimeter-sized calcite crystal in the center (Figure 3h). This calcite phase has abundant pyrite, anhydrite, and fluorite inclusions of up to 25, 50, and 15 μm in size, respectively.

Table 2

Stable Isotope Data From Fracture-Filling Xalcite (FFC), Calcite That Replaced Anhydrite (CRA), Saddle Dolomite (SD), Pyrite (Py), Elemental Sulfur (S), and Quartz (Q)

Drill core	Sample ID	137 Ba		139 La		140 Ce		141 Pr		146 Nd		147 Sm		153 Eu		157 Gd	
		(ppm)	RSD	(ppm)	RSD	(ppm)	RSD	(ppm)	RSD	(ppm)	RSD	(ppm)	RSD	(ppm)	RSD	(ppm)	RSD
FC15-28	C6	6.07	1.2	16.47	0.5	6.63	2.4	1.91	0.4	7.37	0.5	1.24	1.97	0.27	0.9	1.55	1.4
FC13-10	C12	2.12	1.5	4.97	0.6	2.17	1.2	0.62	0.8	2.07	1.0	0.25	1.45	0.06	2.3	0.26	1.8
FC15-28	C5	76.62	0.5	0.28	1.7	0.72	0.9	0.12	1.1	0.58	0.4	0.15	3.84	0.06	2.3	0.17	1.9
FC15-28	C4	15.19	0.1	0.70	1.4	2.31	0.1	0.35	0.5	1.51	1.3	0.39	1.36	0.16	2.6	0.42	1.0
FC15-28	C11	94.91	0.2	0.87	0.7	2.26	1.1	0.29	1.3	1.11	1.3	0.23	4.08	0.08	2.6	0.21	1.7
LR8-11	C9	1346.50	1.1	0.24	1.9	0.26	1.7	0.04	3.6	0.15	1.7	0.04	2.79	x	x	0.05	3.2
LR8-11	C8	286.51	1.0	1.13	0.8	1.27	0.8	0.16	0.6	0.56	1.8	0.10	1.70	x	x	0.10	4.8
LR8-11	C2	139.01	1.2	0.22	0.7	0.63	1.3	0.09	2.7	0.34	2.3	0.08	1.36	x	x	0.06	4.5
FC13-10	A1(C)	72.60	1.9	0.21	1.1	0.49	0.5	0.05	2.2	0.19	2.7	0.05	8.79	x	x	0.06	5.6
FC13-10	A2	5.61	2.1	0.11	2.9	0.25	1.8	0.03	3.5	0.11	1.5	0.02	4.75	x	x	0.02	2.2
LR8-11	C14	961.26	1.0	0.14	1.5	0.24	0.4	0.03	2.5	0.13	4.2	0.03	5.51	x	x	0.04	10.0
FC13-10	A1(F)	320.22	1.3	0.31	1.1	0.73	0.5	0.08	2.3	0.30	2.0	0.08	2.88	x	x	0.10	3.3
FC15-28	C10	638.70	0.8	0.16	2.4	0.37	3.1	0.04	1.1	0.15	4.1	0.04	12.95	x	x	0.03	9.6

		159 Tb		163 Dy		89 Y		165 Ho		166 Er		169 Tm		172 Yb		175 Lu	
drill core	Sample	(ppm)	RSD	(ppm)	RSD	(ppm)	RSD	(ppm)	RSD	(ppm)	RSD	(ppm)	RSD	(ppm)	RSD	(ppm)	RSD
FC15-28	C6	0.218	1.2	1.349	0.7	21.04	1.5	0.293	1.3	0.838	0.7	0.104	0.9	0.608	1.0	0.086	0.8
FC13-10	C12	0.040	3.4	0.215	1.7	2.73	0.6	0.053	3.1	0.157	1.2	0.027	3.5	0.157	2.9	0.029	2.2
FC15-28	C5	0.021	4.0	0.119	2.5	0.92	0.2	0.019	2.9	0.041	4.3	0.002	10.8	0.018	4.9	0.001	13.4
FC15-28	C4	0.062	1.2	0.334	1.3	2.24	0.4	0.055	0.8	0.126	1.6	0.010	6.4	0.053	3.0	0.003	4.1
FC15-28	C11	0.028	1.3	0.149	1.0	0.97	0.3	0.026	1.6	0.068	4.2	0.008	3.7	0.040	4.6	0.006	3.6
LR8-11	C9	0.005	3.3	0.047	5.7	0.89	0.6	0.010	6.0	0.034	2.5	0.003	3.4	0.059	4.2	0.014	3.9
LR8-11	C8	0.011	3.7	0.078	3.8	0.62	0.7	0.013	5.4	0.045	4.1	0.004	6.4	0.044	1.0	0.006	4.2
LR8-11	C2	0.009	4.1	0.046	3.5	0.26	0.5	0.009	4.5	0.023	4.7	0.003	6.3	0.018	12.3	0.004	5.2
FC13-10	A1(C)	0.010	5.8	0.057	2.2	0.75	1.4	0.012	2.7	0.029	3.6	0.003	4.9	0.021	5.9	0.003	14.6
FC13-10	A2	0.003	13.9	0.026	5.3	0.25	1.5	x	x	0.015	0.9	0.002	5.9	0.011	6.4	0.001	15.3
LR8-11	C14	0.004	4.2	0.027	6.5	0.37	1.7	x	x	0.015	4.5	0.002	7.9	0.031	3.3	0.010	3.3
FC13-10	A1(F)	0.018	2.1	0.110	0.6	1.42	1.0	0.021	3.6	0.056	3.1	0.006	3.9	0.045	2.4	0.008	6.6
FC15-28	C10	0.003	9.0	0.020	7.7	0.10	2.4	x	x	0.010	7.6	0.001	5.9	0.020	4.7	0.006	7.5

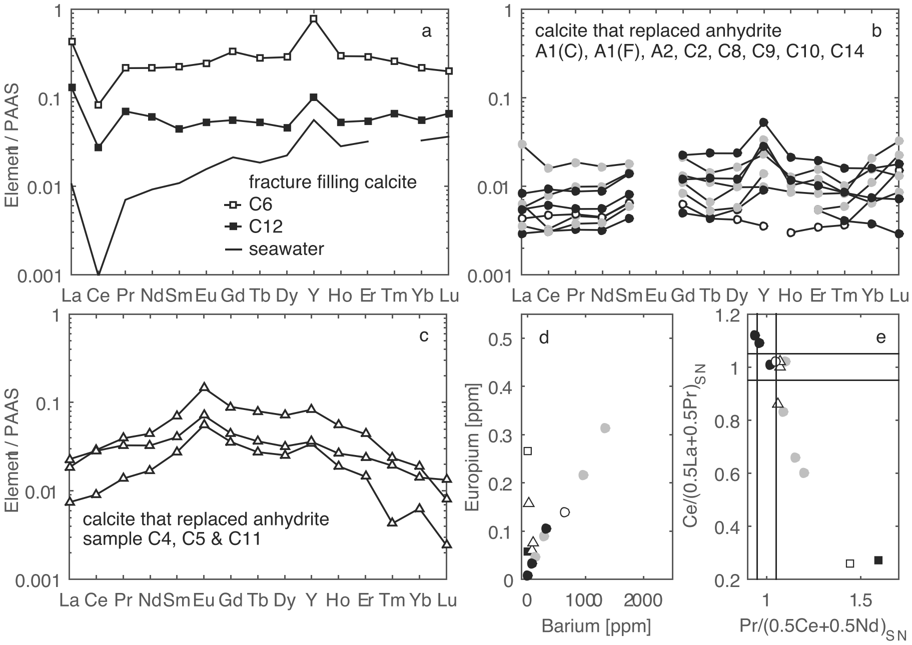

Figure 4. (a–c) Rare earth element patterns from fracture-filling calcite, calcite that replaced anhydrite, three dissimilar calcite that replaced anhydrite samples and seawater (Mitra et al., 1994). (d) Barium and europium concentrations. Squares are fracture-filling calcite samples, whereas circles are calcite that replaced anhydrite samples, and triangles are the three dissimilar calcite that replaced anhydrite samples. The samples from plot (b) correlate in their Ba and Eu concentration, and hence, a severe BaO interference cannot be ruled out. The fracture-filling calcite samples (a) and the three samples from plot (c) lie above the correlation trend and have a reliable Eu concentration. (e) Cerium anomaly diagram from Bau and Dulski (1996). Samples in the bottom right quadrant have true cerium anomalies. The calcite that replaced anhydrite sample with two different calcite textures was analyzed in the core and rim of the nodule and is marked with a black line between the two measurement points. Black, gray, and white symbols represent samples from drill cores FC13-10, LR8-11, and FC15-28, respectively.

Additionally, there are a few <20-μm-sized dolomite, celestine, sylvite, sylvenite, barite, and apatite inclusions. In the chalcedony and quartz-rimmed nodules, the calcite encloses some of the silica crystals.

Pyrite and minor amounts of sphalerite are found at the base of the Madison Formation in all three drill cores and are most abundant in drill core FC15-28. The pyrite and sphalerite form up to 1-mm-sized subhedral to euhedral crystals. Pyrite is precipitated along and within reopened stylolites and is often associated with solid bitumen. In calcite that replaced anhydrite, pyrite is also located within calcite crystals and on crystal boundaries. The pyrite is present as dissemination in the host rock and sometimes overgrows fine dolomite grains. Sphalerite is found precipitated along with pyrite in the same mineral associations but is not present in all sites of pyrite mineralization. Solid bitumen is found as small concretions alongside stylolites, crosscutting fracture-filling calcite and in pores of the calcite that replaced anhydrite. Native sulfur was found in two places: in between calcite that replaced anhydrite crystals in drill core FC15-28 at 2,153.2-m TVD SS (Figure 3g) and within a pyrite and solid bitumen vein in drill core FC13-10 at 1,830.4-m TVD SS (Table 1).

4.2. Rare Earth Elements and Yttrium

All rare earth elements and yttrium (REEY) concentrations are normalized to Post-Archean Average Australian Shale (Table 2). The fracture-filling calcite (samples C6 and C12) and the calcite that replaced anhydrite (C4, C5, C11, A1(C), A1(F), A2, C2, C8, C9, C10, and C14) show distinct REE patterns (Figure 4). The two fracture-filling coarse crystalline calcites (samples C6 and C12) have a flat REEY pattern with distinct negative cerium and positive yttrium anomalies (Figure 4a). The patterns are similar to seawater measurements except for a relative depletion in heavy rare earth elements (HREE) (Mitra et al., 1994; Schmidt et al., 2007; Figure 4a). The Y/Ho ratios for the two samples are 52 and 72, which is in the range of seawater (44–74; Bau & Dulski, 1995). These samples plot in the far right corner of the Ce-Pr-

Table 3
Homogenization Temperatures, Freezing Point Depressions, and Calculated Salinities From Fluid Inclusion Assemblages in Quartz, Fluorite, and Calcite

Well	TVD SS (m)	Th (# FIs; (°C)	Tm ice (°C)	NaCl equivalent salinity (Wt.%)	Mineral	Comments
FC13-10	1,839	140–145(2)	<−15	>18.6	quartz that replaced anhydrite	primaries
		140–145(2)	<−15	>18.6	quartz that replaced anhydrite	primaries
		125–130(3)			quartz that replaced anhydrite	primaries
		115–120(3)			quartz that replaced anhydrite	primaries
		115–120(2)	−16	19.4	quartz that replaced anhydrite	primaries
		115–120(2)	−15	18.6	quartz that replaced anhydrite	primaries
		110–115(5)	<−18	>21	quartz that replaced anhydrite	primaries
		110–115(3)	<−18	>21	quartz that replaced anhydrite	primaries
		110–115(>10)			quartz that replaced anhydrite	primaries
		150–155(4)	>−6	>9.2	quartz that replaced anhydrite	secondaries, later gas-rich inclusions
		170–180(3)	>−6	>9.2	quartz that replaced anhydrite	secondaries, later gas-rich inclusions
		195–200(>10)	−4.2	6.7	calcite that replaced anhydrite	primaries, T_h max
FC13-10	1,914	145–150	<−16	>19.4	fracture-filling calcite	secondaries, T_h max
FC13-10	2,044	155–160	<−16	>19.4	fracture-filling calcite	secondaries, T_h max
FC13-10	2,072	210–215	>−6	<9.2	calcite that replaced anhydrite	secondaries double bubbles clear, T_h max
FC15-28	1,952	195–200	>−6	<9.2	calcite that replaced anhydrite	secondaries, T_h max
FC15-28	1,999	115–120	<−16	>19.4	fracture-filling calcite	secondaries, T_h max
FC15-28	2,010	195–200	>−6	<9.2	calcite that replaced anhydrite	secondaries, T_h max
FC15-28	2,020	135–140	<−18	>21	microspar calcite cement	secondaries, Th max
FC15-28	2,033	135–140	<−18	>21	microspar calcite cement	secondaries, T_h max
FC15-28	2,087	200–215	>−6	<9.2	calcite that replaced anhydrite	secondaries, T_h max
		155–160	<−18	>21	saddle dolomite	primaries, T_h max
FC15-28	2,120	190–195	>−7	<10.5	calcite that replaced anhydrite	primaries, T_h max
		110–115(4)	<−18	>21	fluorite	primaries
		105–110(4)	<−18	>21	fluorite	primaries in last growth zone
		150–160(5)	<−18	>21	fluorite	secondaries
		145–150(5)	<−18	>21	fluorite	secondaries
		120–125(4)	<−18	>21	fluorite	secondaries
		120–125(3)	<−18	>21	fluorite	secondaries
		115–120(>10)	<−18	>21	fluorite	secondaries
		115–120(>10)	<−18	>21	fluorite	secondaries
		105–110(6)	<−18	>21	fluorite	secondaries
		100–110(>100)	−18.6	21.4	fluorite	secondaries
FC15-28	2,125	145–150(>10)	−6.7	10	saddle dolomite	primaries with gas inclusions
FC15-28	2,150	200–215	>−7	<10.5	fluorite	secondaries, lots of gas-filled inclusions
FC15-28	2,201	200–215	−12	16	calcite that replaced anhydrite	secondaries, T_h max
FC15-28	2,203	165–175(5)	−9.2	13.1	quartz	secondaries
		165–175(4)	−12	16	quartz	secondaries
		190–200(>10)			quartz	secondaries
		145–150(4)	−5.1	8	quartz	secondaries
		150–155(3)	−6.8	10.2	quartz	secondaries
		145–150(3)	−9	12.8	quartz	secondaries
		140–145(5)			quartz	secondaries
		195–205(5)	−2.2	3.7	calcite that replaced anhydrite	secondaries
LR8-11	1,390	155–160	<−18	>21	calcite that replaced anhydrite	secondaries, T_h max, clathrate present
		125–135(5)	<−18	>21	quartz	primaries near rim
		125–135(7)	<−18	>21	quartz	primaries near rim
		130–140(4)	<−18	>21	quartz	primaries near rim
		120–130(5)	<−18	>21	quartz	primaries near rim
LR8-11	1,392	160–165	<−18	>21	quartz	primary (possibly), T_h max
		150–160	>−7	<10.5	calcite that replaced anhydrite	secondaries, T_h max
LR8-11	1,393	150–160	<−18	>20	quartz	primaries (possibly)
LR8-11	1,743	180–185	>−7	<10.5	calcite that replaced anhydrite	secondaries, T_h max
LR8-11	1,818	175–180(4)			calcite that replaced anhydrite	primaries
LR8-11	1,942	185–195(3)			calcite that replaced anhydrite	primaries near outer growth zone with gas-filled inclusions
LR8-11	1,984	175–185(4)			calcite that replaced anhydrite	secondaries, abundant gas-filled inclusions present
LR8-11	1,989	205–210	>−6	<9.2	calcite that replaced anhydrite	secondaries, T_h max

Note. Each row represents a distinct fluid inclusion assemblage according to the criteria of Goldstein and Reynolds (1994).
T_h = liquid-vapor homogenization temperature; T_m = final ice melting temperature; salinities calculated from freezing point depression according to equation of Bodnar (1993); clathrate formation upon freezing complicated most freezing point depression measurements, so reported salinities may represent either a minimum (>) or maximum (<) value.

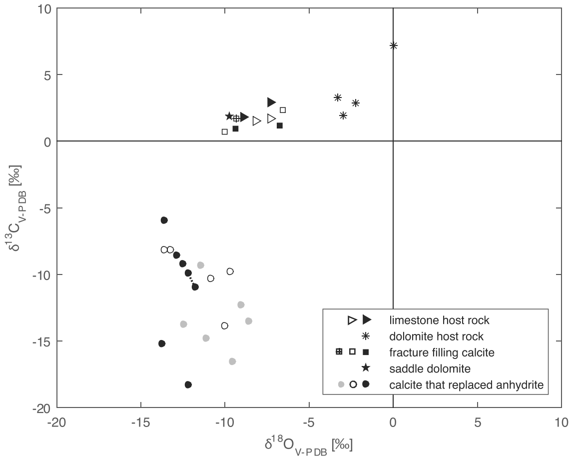

Figure 5. Carbon and oxygen isotopic data from carbonate samples. Sample A1 is marked with a black dotted line between the core (A1(C)) and the rim (A1(F)) measurement. Black, gray, white, and crossed symbols represent samples from drill cores FC13-10, LR8-11, FC15-28, and LR4-22, respectively.

anomaly diagram (Bau & Dulski, 1996), which is in the range of seawater values (Figure 4e). The total concentration in REE in these samples is 65 and 19 ppm.

The REEY patterns of the majority of the calcite that replaced anhydrite samples (A1(C), A1(F), A2, C2, C8, C9, C10, and C14) are characterized by a flat to slightly convex upward shaped pattern with a slight increase from light rare earth elements (LREE) to HREE (Figure 4b). The Y/Ho ratios lie in the range of seawater values (Bau & Dulski, 1995), with the exception of two samples (C2 and C9) that have a Y/Ho ratio of 31 and 89. Three samples (C8, C9, and C14) from drill core LR8-11 plot in the negative cerium anomaly field in the Ce-Pr-anomaly diagram (Bau & Dulski, 1996), whereas the rest of the samples exhibit no cerium anomaly (Figure 4e). The mean absolute REE concentration in these samples is 2 ppm (0.6 to 5.9, *n* = 12). In sample A1 the rim (A1(F)) and core (A1(C)) of the nodule were analyzed and resulted in a very similar REE pattern but the calculated Ce and Pr anomalies shift toward a more positive Ce and more negative Pr anomaly from rim to core (Figure 4e).

Of the samples where calcite replaced anhydrite, there are three samples (C11, C5, and C4) with REE patterns unlike the rest (Figure 4c), all collected from drill core FC15-28 (2,153.9-, 2,202.6-, and 2,202.8-m TVD SS; Figure 1c). They show a convex upward increase in LREE up to europium and a continuous decrease in HREEY with positive europium and yttrium anomalies (Figure 4c). The Y/Ho ratios in these samples are 37, 41, and 49, and they do not have a distinct Cerium anomaly (Bau & Dulski, 1996; Figure 4e). The total concentration in REE in these samples is 4, 9, and 11 ppm.

4.3. Stable Isotopes

The stable isotope data are presented in the order of the paragenetic sequence. Three quartz samples consisting of a siliceous band (sample C3), a silicified breccia (sample Q1), and a quartz nodule (sample Q2) have a very similar oxygen isotopic signature of 28.1‰, 27.5‰, and 28.1‰ V-SMOW, respectively (Table 1). The original limestone samples (L1(1), L1(2), C7(L), and A4(L)) comprise a mean $\delta^{13}C$ value of 2.0‰ V-PDB (1.5‰ to 3‰, *n* = 4) and a mean $\delta^{18}O$ value of −7.9‰ V-PDB (−8.9‰ to −7.3‰, *n* = 4), where *n* is the number of different samples analyzed except for sample L1 where the same sample was sampled twice (Table 1 and Figure 5). The dolomite host rock samples (D1, D2, D3, and D4) have a mean $\delta^{13}C$ value of 3.8‰ V-PDB (2.0‰ to 7.2‰, *n* = 4) and $\delta^{18}O$ value of −2.1‰ V-PDB (−3.3‰ to 0.0‰, *n* = 4; Table 1 and Figure 5). The coarse-grained fracture-filling calcite samples (A4, C12, C6, A5, and LB2) have a positive mean $\delta^{13}C$ value of 1.4‰ V-PDB (0.7‰ to 2.4‰, *n* = 5) and a negative mean $\delta^{18}O$ value of −8.4‰ V-PDB (−10.0‰ to −6.6‰, *n* = 5; Table 1 and Figure 5). The saddle dolomite sample (A4(D)) has $\delta^{13}C$ and $\delta^{18}O$ values of 1.9‰ V-PDB and −9.8‰ V-PDB, respectively (Table 1 and Figure 5). The calcite that replaced anhydrite samples (Table 1) has a distinct negative carbon isotope composition of −11.6‰ V-PDB (−18.3‰ to −5.9‰, *n* = 18) and an oxygen isotope composition of −11.6‰ V-PDB (−13.7‰ to −8.6‰, *n* = 18). Sample A1 shows a higher $\delta^{13}C$ and lower $\delta^{18}O$ value in the rim (sample A1(F)) than in the core (sample A1(C); Table 1 and Figure 5).

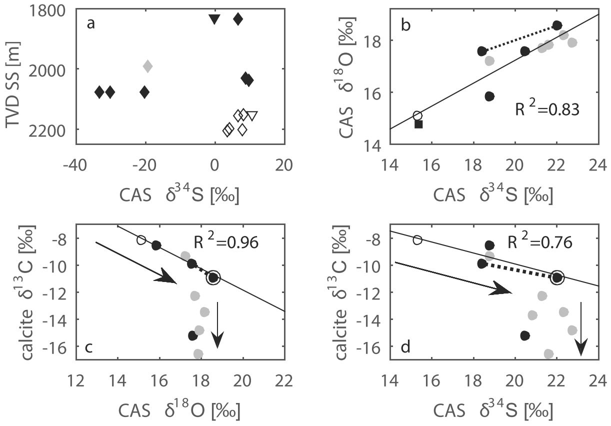

Figure 6. (a) Sulfur isotopes in pyrite (diamonds) and native sulfur (triangles). (b) CAS oxygen and sulfur isotopes in fracture-filling calcite (square) and nodular calcite that replaced anhydrite (circles). There is a strong correlation between the two isotopic values. (c and d) CAS oxygen and sulfur isotopes versus carbon isotopes in calcites that replace anhydrite. Sample A1 is marked with a black line between the core (A1(C)) and the rim (A1(F)) measurement where the core of the sample with a centimeter-seized calcite crystal is marked with a double circle. This double circled sample lies between the two trends indicated by the arrows. Black, gray, and white symbols represent samples from drill cores FC13-10, LR8-11, and FC15-28, respectively.

The pyrite samples seem to form two groups based on their sulfur isotopic signatures ($\delta^{34}S$) (Figure 6a). One sample group (samples P4, P5(1), P5(2), and P11) exhibits a very negative mean $\delta^{34}S$ value of −25.9‰ (−33.2‰ to −19.5‰, *n* = 4), while the remaining samples show positive $\delta^{34}S$ values with a mean of 6.9‰ (3.6‰ to 9.5‰, *n* = 8; Table 1). Two native sulfur samples (samples S1 and S2) have $\delta^{34}S$ values of −0.2‰ and 10.7‰

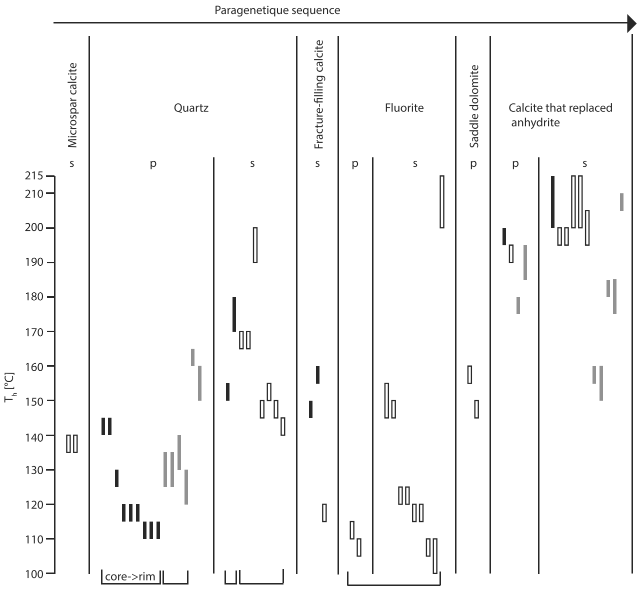

Figure 7. Fluid inclusion homogenization temperatures of primary (p) and secondary (s) fluid inclusion assemblages (FIA) in microspar, quartz, fracture-filling calcite, fluorite, saddle dolomite, and calcite that replaced anhydrite. Samples from drill cores FC13-10, FC15-28, and LR8-11 have black, white, and gray filling colors, respectively. FIA measured in the same sample is bracketed, and in one quartz crystal a transect from core to rim has been measured.

(Table 1 and Figure 6a). The isotopic values of the fracture-filling CAS are δ^{34}S 15.3‰ and δ^{18}O 14.7‰ (Figure 6b). The mean δ^{34}S value of the nodular CAS samples is 20.2‰ (15.3‰ to 22.3‰, $n = 11$), and the associated δ^{18}O value is 17.3‰ (15.1‰ to 18.6‰, $n = 10$; Figure 6b). The nodular CAS sample A1 shows a simultaneous increase in δ^{34}S and δ^{18}O values from rim to core (Figure 6b).

The CAS sulfur and oxygen isotopes exhibit two systematic linear trends when compared to each other and to carbon isotopes. The first trend is from lighter CAS δ^{18}O and δ^{34}S values to heavier ones in the fracture-filling calcite and nodular calcite samples (Figure 6b). This trend has a coefficient of determination (R^2) of 0.83. In the second trend the nodular CAS samples vary from heavier δ^{13}C and lighter δ^{18}O and δ^{34}S values to lighter δ^{13}C and heavier δ^{18}O and δ^{34}S values (Figures 6c and 6d). The observed trend is not linear and exhibits two different slopes (Figures 6c and 6d). At first the CAS δ^{18}O and δ^{34}S increase gradually with decreasing δ^{13}C values but then the trend changes and δ^{13}C values decrease with almost no change in CAS δ^{18}O and δ^{34}S values. The gradual change of δ^{13}C with CAS δ^{18}O and δ^{34}S values exhibits an R^2 of 0.96 and 0.76, respectively.

4.4. Fluid Inclusions

Homogenization temperatures (T_h) and freezing point depressions (T_m ice) of primary and secondary aqueous fluid inclusion assemblages hosted in microspar, quartz, fracture-filling calcite, fluorite, saddle dolomite, and calcite that replaced anhydrite were measured in core samples from three wells (Figure 7 and Table 3).

The analyzed quartz samples tend to have an euhedral crystal habit with a cloudy inclusion-rich core followed by a clear, relatively inclusion-free rim. In drill core FC13-10, T_h values of primary inclusions decrease from ~140 °C–145 °C in the cloudy core to ~115 °C at the boundary with the clear rim, indicating a temperature drop during quartz precipitation (Figure 7). In FC15-28 fluorite-hosted primary fluid inclusions have T_h values of 105 °C to 115 °C, very similar to the temperatures in the outer growth zone of euhedral quartz. This suggests that these phases may have formed close in time to each other. Primary fluid inclusions in calcite that replaced anhydrite have T_h of ≥175 °C (Table 3). Following crystallization of all phases, secondary fluid inclusion assemblages hosted in quartz, fluorite, and calcite indicate that fluids with a maximum temperature of ~210 °C–215 °C migrated through the Madison Formation (Table 3 and Figure 7).

Fluid inclusion salinities are generally significantly higher than seawater (Table 3). Primary inclusions in quartz and fluorite almost ubiquitously have salinities in excess of 21 weight % (NaCl equivalent). However, primary inclusions in calcite that replaced anhydrite and secondary inclusions in quartz and calcite that replaced anhydrite tend to have lower salinities. The final ice-melting temperature of many of these later inclusions was difficult to measure due to a high concentration of $CH_4 \pm CO_2 \pm H_2S$ dissolved in the water resulting in clathrate formation upon freezing. Thus, some salinity values represent a maximum, rather than absolute, value (see Table 3). Regardless, these salinities are lower than the salinities found in primary inclusions in quartz and fluorite (Table 3).

5. Data Interpretation

5.1. Paragenetic Sequence

The observed limestone texture and composition are consistent with the interpretation that the Madison Formation was deposited in a shallow water, subtidal setting (Gutschick & Sandberg, 1983; Sando, 1976). Dolomitization has been interpreted to have occurred during early burial by seepage and reflux of hypersaline brines (Moore, 1995, 2001; Smith, 1991; Sonnenfeld, 1996a), and the observations made in this study are consistent with that interpretation. On the basis that quartz replaces the dolomitic breccia and is enveloped by fracture-filling calcite, quartz and silica are interpreted to have formed before the fracture-filling calcite.

The small variation in oxygen isotopic values from the silica phases suggests that precipitation occurred from a single fluid in a narrow time range. The decreasing fluid inclusion homogenization temperatures from core to rim in the quartz-replaced anhydrite nodule suggests precipitation from a hydrothermal fluid that cooled from 165 °C to potentially ambient temperatures of 115 °C (Table 3). Subsequently, some microfractures developed and were occluded by fracture-filling calcite, most likely from the same fluid as the quartz.

Fluorite inclusions were observed alongside anhydrite in quartz replacing anhydrite and in calcite that replaced anhydrite. This suggests that the first fluorite phase was evaporitic in origin, in agreement with observations in dolomitic rocks of the Florida aquifer (Cook et al., 1985). The source for the second fluorite phase, occurring as a single vein and postdating the fracture-filling calcite, is likely external in origin. The fluid inclusion homogenization temperature of this vein fits with the interpretation of a brine cooling to ambient temperature of 105 °C–115 °C and precipitating quartz, fracture-filling calcite, and then fluorite. The saddle dolomite postdates the fracture-filling calcite since the dolomite crystals enclose some fracture-filling calcite crystals.

The last precipitating phase of calcite is that which replaced anhydrite. The observation of large crystals in the center of the nodules suggests that the anhydrite was replaced from rim toward the core, which is consistent with observations elsewhere (Alonso-Zarza et al., 2002; Hesse, 1989; Milliken, 1979; Worden & Smalgeoley, 1996). Pyrite and minor amounts of sphalerite are precipitated along grain boundaries and enclosed within calcite crystals that replaced anhydrite, implying contemporaneous formation. Solid bitumen and native sulfur precipitated either contemporaneously or later than the calcite that replaced anhydrite since they are precipitated in between calcite crystals.

5.2. Evidence for TSR

Evidence for in situ sulfate reduction at the LaBarge Field comes from the identification of various reduced sulfur phases including native sulfur, pyrite, sphalerite, and H_2S. In addition, other known by-products of sulfur reduction were observed, including calcite that replaced anhydrite and solid bitumen (Kelemen et al., 2010; Kendall, 2001; King et al., 2014; Machel, 2001), which are related in time and space to the reduced sulfur phases.

Depending on the reaction temperature, sulfate reduction is usually caused by either bacterial or thermochemical sulfate reduction (Machel, 2001, and references therein). To explain the presence of solid bitumen, oil had to be present in the reservoir at some time prior to or concomitant with sulfate reduction. Oil is reported to have migrated into the Madison Formation around 76–84 Ma ago (Roberts et al., 2005). At that time the formation temperature was approximately 115 °C–145 °C based on the thermal history reported by Roberts et al. (2005)). During and after oil migration into the LaBarge field, the formation temperature was too high (>80 °C) for bacterial sulfate reduction (BSR) (Machel, 2001, and references therein). Fluid inclusion data infer precipitation temperatures of >175 °C for the calcite that replaced anhydrite and therefore also exclude BSR as a sulfate reduction mechanism (Table 3). In addition, the gas composition at the LaBarge Field is more analogous to other systems with ≥5%–10% H_2S that is reported to be a product of TSR rather than BSR (Machel, 2001, and references therein).

5.3. Rare Earth Elements

Calcite REEY patterns are influenced by the fluid composition and physicochemical precipitation conditions (Bau & Möller, 1992). In sedimentary carbonate reservoirs the REEY pattern of the precursor limestone can be preserved during diagenesis and dolomitization under low and moderate fluid-rock ratios (Banner et al., 1988). The fracture-filling calcite samples have similar REEY patterns to seawater, with characteristic Ce and Y/Ho anomalies (Figure 4a). Their lower HREE abundance compared to seawater could arise from the decreasing compatibility of HREE that are incorporated in diagenetic calcite, compared to LREE (Figure 4a; Tanaka & Kawabe, 2006; Zhong & Mucci, 1995). The cerium anomaly calculated by the method of Bau and Dulski (1996) can indicate the oxidation state of the fluid at the time of the calcite precipitation (Figure 4e). Under oxic conditions cerium is oxidized to the immobile ion Ce^{4+}, and hence, the fluid will have a depleted cerium concentration. Alternatively, the cerium anomaly can be derived from the host rock during fluid-rock interaction. The REEY pattern and the cerium anomaly of the fracture-filling calcite are likely inherited from the host rock probably through recrystallization of the microspar. Further support for this comes from oxygen isotopic data, which will be discussed in the next section.

The majority of calcite that replaced anhydrite samples have flat REEY pattern with Y/Ho ratios mainly in the range of seawater, a low to nonexistent cerium anomaly, and an order of magnitude lower concentration of REE than fracture-filling calcite samples. The Y/Ho ratios suggest that the fluid inherited the Y/Ho during replacement of anhydrite. The two Y/Ho ratios that are slightly above and below seawater values are harder to explain. The calculated cerium anomalies in these samples lie on a trend from negative Ce and positive Pr anomalies to no Ce and Pr anomalies, which indicates a trend toward a more reducing environment (Figure 4e). This trend is also seen in sample A1, which shows more reducing conditions from the rim (A1(F)) to the core (A1(C)) of the sample.

Additionally, there are three anhydrite replacing calcite phases (sample C4, C5, and C11) that show convex upward shaped REEY patterns with positive Eu and Y/Ho anomalies. Convex upward shaped REE patterns have been documented for many hydrothermal waters and carbonates that formed from acidic crustal fluids (Bau & Möller, 1992; Hecht et al., 1999; Lüders et al., 1993; Michard, 1989; Möller, 1983; Ohr et al., 1994). In these studies, the fluids most likely originated from interactions with pelitic metasediments or gneisses under acidic conditions whereby apatite is mobilized (Hecht et al., 1999; Möller et al., 1997; Ohr et al., 1994). Yttrium and holmium exhibit a similar geochemical behavior and therefore remain coupled during many geochemical processes (Bau & Dulski, 1999; Jochum et al., 1986). Volcanic and detrital rocks exhibit chondritic Y/Ho ratios of 28 (Bau, 1996; Jochum et al., 1986), and therefore, crustal fluids exhibit chondritic rather than superchondritic Y/Ho ratios (>28). The superchondritic values of the three dissimilar calcites that replaced anhydrite, however, could have formed during fluid advection, whereby Y is less adsorbed than any other trivalent REE (Möller, 1997; Möller et al., 2004). An excess of Eu relative to the neighboring REE is generated during water-rock interaction at temperatures >200 °C (Bau, 1991; Sverjensky, 1984). Under these conditions the Eu ions are reduced to Eu^{2+}, which are less susceptible to sorption and preferentially transported in the fluid (Bau, 1991; Bau & Möller, 1992). The Eu anomaly remains even if the fluids migrate into a cooler, oxidizing region where Eu^{3+} is incorporated into the precipitating calcite (Bau et al., 2010). Eu^{3+} is preferentially incorporated into calcite due to its smaller ionic radius compared to Eu^{2+} (Lüders et al., 1993). The production of a positive Eu anomaly without high-temperature water-rock interaction is unlikely due to the low-oxygen fugacity required to reduce Eu^{2+} at low temperature (Bau, 1991; Bau & Möller, 1992), except when the H_2S concentration exceeds the SO_4^{2-} concentration in the fluid (Lüders et al., 1993; Möller, 1983). Positive Eu anomalies could even be produced in closed system basins if burial temperatures exceed 200 °C and fluid-rock interaction occurs (Jiang et al., 2015). In the LaBarge Field the maximum estimated burial depth of the base of the Madison Formation was 6,600 m. When interpreted in the context of a known geothermal gradient of 28.8 °C/km and surface temperatures of 25 °C, this yields a maximum burial temperature of 215 °C (Figure 2; Roberts et al., 2005). This temperature is above the 200 °C required for an Eu anomaly in a closed system. Alternatively, it is possible that the observed positive Eu anomalies are related to a hydrothermal fluid. There is no distinct cerium anomaly measured in these samples, which indicates precipitation under reducing conditions. In conclusion, these three samples indicate a different fluid at a different time in the system.

5.4. Carbon and Oxygen Isotopes and Fluid Temperatures

The limestone host rock at the LaBarge Field has a carbon and oxygen isotopic signature consistent with other measurements of the Mississippian Madison Formation in Wyoming (e.g., $\delta^{13}C$ 0.5‰ to 6.5‰, $\delta^{18}O$ −5.5‰ to −1‰; Budai & Cummings, 1987; and $\delta^{13}C$ −3‰ to 7‰, $\delta^{18}O$ −9‰ to 3‰; Katz et al., 2006). The Mississippian seawater oxygen isotopic composition has been estimated to be between −1‰ and −5.3‰ V-SMOW (Came et al., 2007; Veizer et al., 2000; Wallmann, 2004), which equates to a limestone of −3.7‰ to −7.8‰ V-PDB at a typical precipitation temperature of 25 °C (Kim & O'Neil, 1997). The oxygen isotope of the limestone at the LaBarge Field (−7.3‰ to −8.9‰ V-PDB) is lighter than these estimates, and therefore, another process likely modified the original composition. The oxygen isotopic composition of the fracture-filling calcite, however, overlaps with those of the limestone, which suggests that the microspar recrystallized during the precipitation of the fracture-filling calcite and hence lowered the limestone's oxygen isotope value (Figure 5). This is in agreement with the seawater like REE composition of the fracture-filling calcite inherited from interaction with the microspar. The carbon and oxygen isotopes of the dolomite host rock are consistent with previous observations of the Madison Formation where the dolomite was interpreted to have formed as early diagenetic phase by reflux of hypersaline brines (e.g., $\delta^{13}C$ 0.5‰

to 4.1‰, δ^{18}O −3.2‰ to 1‰; Budai et al., 1984; Smith, 1991; δ^{13}C −1‰ to 6.9‰, δ^{18}O −8.5‰ to 3‰; Smith et al., 2004; and δ^{13}C −2.9‰ to 7.1‰, δ^{18}O −8.9‰ to 6.3‰; Katz, 2008).

To integrate the fluid origins of the different phases, the fluid compositions were calculated based on the mineral δ^{18}O composition combined with the fluid inclusion microthermometry data. The anhydrite-replacement quartz (sample Q2), with an oxygen isotope composition of 28.1‰, is in equilibrium with a fluid ranging from 12.2‰ to 8.5‰ V-SMOW at the inferred precipitation temperatures from primary fluid inclusion homogenization temperatures in quartz from 145 °C to 115 °C (Clayton et al., 1972). Since the fluid inclusion homogenization temperatures in quartz decrease from core to rim and exhibit a high salinity, the quartz likely precipitated from an external fluid with an isotopically heavy composition, such as a basinal brine that was mobilized through laramide deformation.

As discussed above, fracture-filling calcite precipitation postdates quartz precipitation but predates the precipitation of fluorite in the vein. Given that there are independent constraints on the precipitation temperature of quartz at 145 °C–115 °C and a well-defined paragenesis, it can be assumed that the fracture-filling calcite precipitated at a similar temperature to that of the quartz. If the fracture-filling calcite did precipitate at a temperature of 115 °C, it would have precipitated from a fluid with an oxygen isotope composition of 7.6‰ V-SMOW (Kim & O'Neil, 1997) based on the average measured isotopic signature of the four samples. This is close to the lowest value calculated from the last precipitating quartz sample and suggests that these phases precipitated from a common pore fluid. Furthermore, the similar carbon isotopic composition of the fracture-filling calcite to that of the Madison Formation host rock suggests that this calcite precipitated from a fluid in equilibrium with the host rock with moderate to low fluid-rock ratios (Sheppard & Schwarz, 1970).

The carbon isotopic value of the saddle dolomite (1.9‰) suggests that it also precipitated from a fluid in equilibrium with the host rock because of the overlap in their isotopic signatures (Table 1). The saddle dolomite postdates the fracture-filling calcite, with primary fluid inclusion homogenization temperatures demonstrating that this precipitated at 145 °C–160 °C. A fluid in equilibrium with the oxygen isotopic value of the saddle dolomite at these temperatures would have a heavy isotopic composition, between 7.9‰ and 9.6‰ V-SMOW (Kim & O'Neil, 1997; Sheppard & Schwarz, 1970). These values are within the range of those estimated for the precipitation of quartz and fracture-filling calcite, again indicative of precipitation from a common pore fluid at increasingly elevated temperatures.

The carbon and oxygen isotopes of the calcite that replaced anhydrite form a distinct group. The carbon isotopes of the calcite that replaced anhydrite samples are strikingly clustered at <−5‰ and are all at least 5‰ lighter than the host rock (Figure 5). This large difference between the host rock and the calcite that replaced anhydrite indicates that there must have been a source of isotopically light carbon in the fluid when this calcite phase precipitated. Potential sources of isotopically light carbon at the temperatures at which calcite replacement of anhydrite took place (175 °C–200 °C based on fluid inclusion homogenization temperatures) include hydrocarbons or carbon dioxide. The oxygen isotope values of these samples cluster between average host rock values and much lower values of up to −13.7‰ V-PDB. The low-oxygen isotopic values could have originated from either precipitation at increasingly elevated temperatures or precipitation from an isotopically light fluid. The most common, volumetrically abundant, isotopically light diagenetic fluid is meteoric water, but given that this precipitation occurred at burial depths of several kilometers, this is highly unlikely. Using the average oxygen isotopic composition and the fluid inclusion homogenization temperatures (175 °C–200 °C) of anhydrite replacement calcite, the oxygen isotopic composition of the fluid from which this cement precipitated was estimated to be 10.7‰ to 12.9‰ (V-SMOW; Kim & O'Neil, 1997). It is unclear from the stable isotopes alone if this isotopically heavy fluid could either be an external crustal fluid or the result of fluid-rock interaction of indigenous formation water at high temperatures.

5.5. CAS Stable Isotope Fractionation in TSR

The CAS isotopic signature of the fracture-filling calcites are interpreted to record the sulfate present in the reservoir prior to TSR as their values lie in the range of Mississippian seawater of δ^{34}S 14‰–21.5‰ and δ^{18}O 14‰–18‰ (Claypool et al., 1980; Kampschulte et al., 2001; Kampschulte & Strauss, 2004). This suggests that the Mississippian anhydrites were controlling the aqueous sulfate prior to TSR (Figure 6b). The nodular CAS sample with the lowest δ^{34}S and δ^{18}O isotopic values (sample C10) exhibits an isotopic composition very close to the fracture-filling calcite sample (sample C12) and supports the previous inference that the Mississippian sulfate source dominated when the TSR process started. An additional influx of dissolved sulfate from the overlying Permian Phosphoria Formation characterized by much lower sulfur and oxygen isotopic values has been suggested previously (King et al., 2014), but this is not supported by the CAS data presented here (Figure 6b).

The variation and correlation between sulfur and oxygen isotopes in CAS can be caused by primary (sedimentary) or secondary diagenetic processes. In the first case, the isotopic signature would be indicative of evaporite precipitation prior to burial. However, the fractionation is negligible between seawater sulfate and the precipitating anhydrite (Burdett et al., 1989; Kampschulte et al., 2001; Kampschulte & Strauss, 2004; Newton et al., 2004), and hence, no isotopic difference would be expected between the different samples. Support for this comes from the observation that only a few anhydrite microinclusions are present in the calcite that replaced anhydrite. Hence, most of the CAS is interpreted to be lattice bound sulfate that was incorporated into the precipitating calcite. Consequently, the isotopic composition of CAS represents the sulfate composition of the fluid at the time of calcite replacement. As such, there is no plausible explanation for a primary origin of the isotopic covariation in the CAS (Figure 6b).

The second possibility for the correlation of the oxygen and sulfur isotopes is a secondary process such as BSR or TSR. In redox reactions such as these, the isotopic values of the source material increase successively with continuous reaction progress due to the preferential reaction of the lighter isotopes (a normal isotope effect), enriching the residual source material in the heavier isotope. In BSR systems, increasing isotopic values with increasing depth have been observed and related to increasing reaction progression (Aharon & Fu, 2000, 2003; Antler et al., 2013; Böttcher et al., 1998; Fritz et al., 1989; Strebel et al., 1990). In these systems, a linear correlation between δ^{34}S and δ^{18}O isotopes has been attributed to kinetic fractionation of oxygen and sulfur isotopes during the same reaction step (Aharon & Fu, 2000, 2003; Antler et al., 2013). Kinetic fractionation of sulfur isotopes during TSR has also been observed experimentally (Cross et al., 2004; Kiyosu, 1980; Kiyosu & Krouse, 1990, 1993; Meshoulam et al., 2016). In the LaBarge Field, TSR is the dominant sulfate reduction process that fractionated the sulfate. The slope of the correlation between the CAS oxygen and sulfur isotopes (δ^{18}O/δ^{34}S) is 0.53, which means that the sulfur fractionation is almost double that of oxygen (Figure 6b).

Further isotopic variation caused by TSR can be found among the products of the redox reaction. The calcite that replaced anhydrite exhibits a trend from heavier δ^{13}C and lighter δ^{18}O and δ^{34}S values to lighter δ^{13}C and heavier δ^{18}O and δ^{34}S values (Figures 6c and 6d). In the first segment (upper arrow in Figures 6c and 6d) the decrease in δ^{13}C values could arise from mixing of the carbon already present in the pore water (as HCO_3^-) with an isotopically light carbon (as CO_2(g)) produced as a by-product of TSR. This is in agreement with the simultaneous increase in CAS δ^{18}O and δ^{34}S that arose as a result of the progressive distillation of these isotopes during TSR. A similar trend has been observed in other TSR reservoirs where decreasing δ^{13}C values in calcite have been attributed to an increased extent of anhydrite reaction (Machel et al., 1995; Worden & Smalgeoley, 1996) and decreasing δ^{13}C values in water have been associated with the progress of TSR (Wynn et al., 2010). Sample A1 that has been analyzed in the rim and core is in agreement with this observed trend and records an evolving fluid composition at two different times. The carbon and CAS isotopic data of sample A1(C) plot at the intersection of the two observed trends (circled sample in Figures 6c and 6d). The growth of the large calcite crystal in this sample reflects slower precipitation near equilibrium and therefore could represent the termination of the TSR process in this system.

In the second segment (lower arrow in Figures 6c and 6d) the continuous decrease in δ^{13}C is not accompanied by a continuous increase in CAS δ^{18}O and δ^{34}S. This shift in isotope evolution was attributed to be associated with fluid mixing with an external carbon source that is not connected to the TSR process (Figures 6c and 6d). The addition of isotopically light or hot CO_2 will change the carbon isotopic composition of the fluid but will not have an influence on the sulfate isotopic composition of the fluid since the isotope exchange reaction between dissolved sulfate and water is extremely slow (Llyod, 1967). The δ^{13}C of the CO_2(g) present today in the LaBarge Field has an average value of −5.2‰ (−5.45‰ to −5.02‰, $n = 8$; Frost, 2011) and is in equilibrium with the isotopically lightest calcites at 210 °C (Clark & Fritz, 1997; Romanek et al., 1992; Sheppard & Schwarz, 1970). This segment might record a formation fluid no longer influenced by TSR but instead by the influx of CO_2. There is not enough resolution or data to unambiguously determine whether the hydrothermal CO_2 arrived prior to, during or after TSR, although it seems unlikely that it entered prior or during TSR because of the apparent equilibrium precipitation of the large crystals that precede the onset of precipitation of isotopically lighter calcite (Figures 6c and 6d).

Other products of TSR in the LaBarge Field are H_2S and the metal sulfides that potentially precipitated from it. In a closed system the kinetic fractionation of TSR can be described as a Rayleigh-type fractionation process (Kiyosu & Krouse, 1990). Starting with an initial sulfate isotopic composition of 15.3‰ and a H_2S(g) in equilibrium with the pyrite with the lowest positive $\delta^{34}S$ value of +3.6‰ (Ohmoto & Rye, 1979), the temperature at which the fractionation factor matches these numbers can be inferred. The fractionation factor Py-$SO^{2-}{}_4$(aq) is −11.7 (Kiyosu & Krouse, 1990; Ohmoto & Rye, 1979) at a temperature of 155 °C. The successive increase in $\delta^{34}S$ of subsequent pyrite phases could then be explained by formation from an increasingly isotopically enriched H_2S. The accumulated H_2S would reach the observed $\delta^{34}S$ value of 10‰ (King et al., 2014) after over 80% of the sulfate is consumed. In the temperature range of TSR (>100 °C; Machel, 2001), the fractionation between sulfate and sulfide is not large enough to form isotopically negative pyrites, which have been identified in two of the cores (Kiyosu & Krouse, 1990). Even though there is no petrographic indication or other evidence for bacterial sulfate reduction, these isotopically negative pyrites have likely formed diagenetically below 80 °C (Machel, 2001, and references therein).

6. Discussion

6.1. Sulfur Cycling and Duration of TSR

Sulfur cycling in the LaBarge Field can be traced by estimating source and sink material affected by TSR. The gross rock volume of the LaBarge reservoir is estimated to be 1,400 km^3 based on a reservoir map (Stilwell, 1989; Figure 1b). The average porosity is 9% (Huang et al., 2007), which yields a total pore volume of 126 km^3. An estimated volume of former anhydrite nodules in the drill cores of 0.2 vol% would equate to 2.55×10^9 m^3 or 5.6×10^{13} mol in the reservoir. The amount of CO_2 is estimated to be $3.15 \times 10^{+12}$ m^3 STP (De Bruin, 1991; Lynds, 2010). Based on an assumed CO_2-H_2S ratio of 1:13 (gas composition of 65% CO_2 and 5% H_2S; Huang et al., 2007) and this CO_2 volume, the H_2S gas volume is calculated to be 2.4×10^{11} m^3 or 9.8×10^{12} mol. The amount of anhydrite therefore exceeds the amount of H_2S by a factor 6. The overall TSR reaction ($CaSO_4 + HC \geq H_2S + CaCO_3/CO_2$ + solid bitumen + altered HC + H_2O) would yield 1 mol of H_2S for each mol of reacted anhydrite (Goldhaber & Orr, 1995; Machel, 1987b; Orr, 1974). Therefore, it is likely that the H_2S found in the Madison Formation in the LaBarge Field has been produced from the dissolved local anhydrite without an external sulfate source even though no primary anhydrite is left. It is proposed that dissolved sulfate remained abundant in the fluid since calcite that precipitated after TSR also contains sulfate and present day fluids hold 10,000 mg/L $SO_4{}^{2-}$ (Blondes et al., 2014). The discrepancy between the amount of anhydrite and H_2S could be associated with spatial heterogeneity in the anhydrite content of the Madison Formation, with H_2S migration out of the reservoir or another reason for anhydrite dissolution unrelated to sulfate reduction. Alternatively, it could be explained by sulfide precipitation, which consumes 2 mol of H_2S for each mole of pyrite precipitated. The amount of pyrite estimated through logging of the three drill cores is approximately 10 ppm and equates to $4 \times 10^{+4}$ mol and results in $8 \times 10^{+4}$ mol of H_2S consumed. This suggests that sulfide precipitation played a subordinate role in reducing the amount of H_2S in the reservoir, compared to the $9.8 \times 10^{+12}$ mol of H_2S present today.

The kinetics and duration of TSR are not well understood (Machel, 2001). Due to the extensive fractionation in $\delta^{34}S_{sulfate}$, the rate limiting step was likely the reduction rather than sulfate dissolution (Figure 6b; Meshoulam et al., 2016). Goldhaber and Orr (1995) estimated a rate for the reduction step of 10^{-6} mol of sulfate per liter per year for high H_2S systems at 150 °C. In the LaBarge Field the amount of reacted sulfate is at least the equivalent of the total amount of H_2S (9.8×10^{12} mol). Assuming a total pore space of $1.26*10^{10}$ m^3 (Huang et al., 2007; Stilwell, 1989) filled with water, the pore fluid would have had a sulfate concentration of 0.8 mol/L. This concentration would take approximately 80 ka to react (Goldhaber & Orr, 1995). The reaction time could increase if there was a higher initial sulfate concentration or decrease if the TSR process occurred at a higher temperature than 150 °C. Aqueous fluid inclusions in calcite that replaced anhydrite (>175 °C) provide good evidence that temperatures exceeded 150 °C (i.e., up to 200 °C; Figure 7), and as such, this time represents an upper limit on the likely duration of TSR in the LaBarge Field.

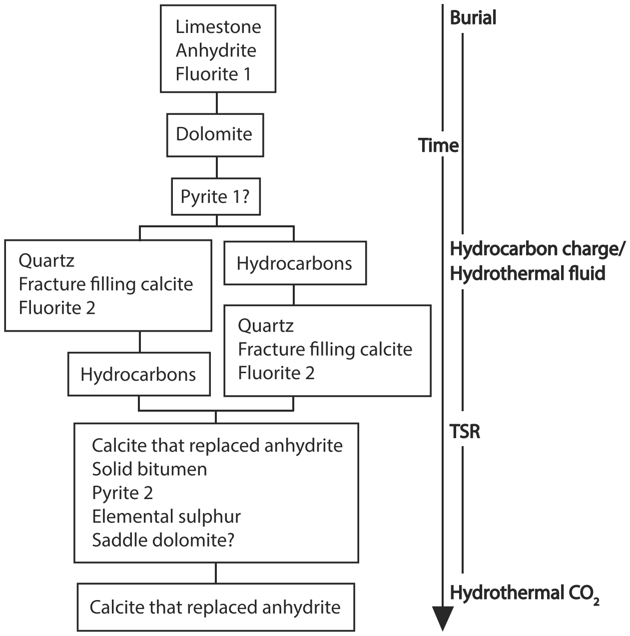

Figure 8. Precipitated mineral phases and fluid inputs with increasing time.

6.2. Fluid Sources and Timing of TSR

The composition of the main fluid phases that circulated in the reservoir is recorded in the fracture-filling calcite, the solid bitumen, and the calcite that replaced anhydrite (Figure 8). The fracture-filling calcite cement most likely precipitated from a saline brine following quartz precipitation. This is supported by the quartz fluid inclusion homogenization temperatures showing decreasing temperatures from the core of the crystals to the rim (Figure 7).

During or following fracture-filling calcite precipitation, the reservoir was charged with oil from the overlying Phosphoria Formation (Johnson, 2005; Figure 8). The calcite that replaced anhydrite formed after the influx of oil and the start of TSR, indicated by the low carbon isotopic values, the more reducing conditions indicated by the lack of negative cerium anomalies, and the solid bitumen coprecipitation/postprecipitation. TSR progressed in the reservoir and altered the fluid composition as suggested by the increase in CAS isotopic values with decreasing carbon isotopic values. At some point, TSR ceased and the fluid composition remained stable and close to equilibrium for some time, reflected in the development of large crystals in the core of some calcite that replaced anhydrite nodules. There is no direct evidence of the limiting factor that caused the TSR process in the LaBarge Field to cease, but a likely explanation is that the heavy hydrocarbons were totally consumed and the reaction could not progress with methane as the only organic source left in the reservoir (Amrani et al., 2008; Machel, 2001, and references therein). The excess of a reaction product, however, could also have halted the reaction. This raises the possibility of a pause between TSR and the influx of the CO_2 and suggests that the influx of CO_2 did not influence the progression of TSR in the LaBarge Field.

Following TSR, hydrothermal CO_2 is interpreted to have flooded the reservoir, reflected in the decreasing carbon isotopic composition with limited variation in the CAS isotopic composition in some of the calcite that replaced anhydrite samples (Figures 6c and 6d). The gaseous CO_2 that currently occupies the reservoir is in equilibrium with the lightest carbon isotope signatures in calcite at a temperature of 210 °C (Clark & Fritz, 1997; Romanek et al., 1992; Sheppard & Schwarz, 1970). Indeed, the observed positive Eu anomalies and the convex upward shaped REE pattern in three of the calcite that replaced anhydrite samples indicate the presence of an acidic hydrothermal fluid and are therefore probably related to the external CO_2 influx. The three calcite phases that replaced anhydrite samples from drill core FC15-28 are the deepest samples (2,150- to 2,200-m TVD SS) and are located next to a basement-involved reverse fault (Kraig et al., 1987); hence, the fluid might have entered the reservoir along this fault (Stilwell, 1989). This interpretation is supported by the observation that CO_2 concentration increases toward the base of the reservoir and toward this fault (Stilwell, 1989). The source of the CO_2, however, remains uncertain; the CO_2 has a $\delta^{13}C$ and a $^3He/CO_2$ ratio in mantle range (Frost, 2011; Merrill et al., 2014), yet there is no evidence that a magmatic fluid could have produced the convex upward shaped REE pattern with a positive Eu anomaly (Banks et al., 1994) unless it interacted with metasediments along the flow path.

7. Conclusion

1. Mineralogical and petrographical observations, along with the burial history and fluid inclusion data, argue for in situ TSR in the LaBarge Field.
2. It has been shown that sulfate sulfur and oxygen isotopes cofractionated during the TSR process. This indicates a fractionation in the same reaction step during which the sulfur isotopes fractionate almost twice the amount of the oxygen isotopes. The CAS isotopic data also reveal that a single Mississippian sulfate source was involved in TSR.
3. The progression of the TSR reaction is illustrated by the cofractionation in CAS isotopes to higher values, accompanied by a decreasing $\delta^{13}C$ value. The end of TSR is marked by the precipitation of large calcite crystals in the core of some calcite that replaced anhydrite nodules.

4. The limiting factor for TSR is likely the exhaustion of heavy hydrocarbons since mass balance calculations and present-day pore fluid analyses suggest that dissolved sulfate occurred in excess.
5. The approximate length of TSR is 80 ka, based on a reaction rate from Goldhaber and Orr (1995) and the assumption of a reaction step limiting system due to the extensive sulfate fractionation (Meshoulam et al., 2016). Depending on the reservoir age, dating techniques could also provide useful constraints about the duration of the TSR process at the LaBarge Field.
6. An influx of an external source of CO_2 after the cessation of TSR is marked by a trend of decreasing $\delta^{13}C$ with limited changes in CAS isotopic values. This suggests that the influx of CO_2 did not influence the TSR process. A possible entry point for the CO_2 could be located along the reverse fault on the west side of the field based on observations from REE data. The source of the CO_2 remains controversial; however, future Nd isotopic measurements could help to distinguish between a mantle and a crustal origin of CO_2 and lead to a better understanding of the timing of the CO_2 influx and narrow the age and temperature range of the TSR process.
7. Altogether, it has been shown that the combination of petrography, REE, fluid inclusion, and stable isotope measurements can be useful to disentangle the fluid history of a large reservoir and could help to predict the occurrence and magnitude of TSR elsewhere.

Appendix A: Sample C14 (Left) and A1 (Right): Calcite That Replaced Anhydrite With Anhydrite Microinclusions.

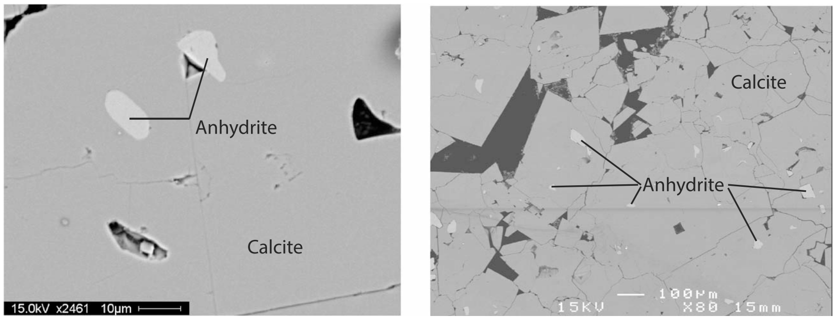

Acknowledgments

Thanks to Thomas Becker at ExxonMobil for discussions on the burial history of the LaBarge Field. We would like to thank Peter Wynn at Lancaster University for discussions about the CAS methodology and Dave Hughes at Lancaster University for helping with the stable isotope measurements. Further, we acknowledge Alison Mc Donald from the Scottish Universities Environmental Research Centre for her support with the pyrite isotopic analysis. We also thank Paul Lythgoe at the University of Manchester for conducting the rare earth element measurements. This work was supported by the University of Manchester and Lancaster University. The data used can be found in Tables 1–3.

References

Aharon, P., & Fu, B. (2000). Microbial sulfate reduction rates and sulfur and oxygen isotope fractionations at oil and gas seeps in deepwater Gulf of Mexico. *Geochimica et Cosmochimica Acta*, *64*(2), 233–246. https://doi.org/10.1016/S0016-7037(99)00292-6

Aharon, P., & Fu, B. (2003). Sulfur and oxygen isotopes of coeval sulfate–sulfide in pore fluids of cold seep sediments with sharp redox gradients. *Chemical Geology*, *195*(1–4), 201–218. https://doi.org/10.1016/S0009-2541(02)00395-9

Allis, R., Chidsey, T., Gwynn, W., Morgan, C., White, S., Adams, M., & Moore, J. (2001). Natural CO_2 reservoirs on the Colorado Plateau and southern Rocky Mountains: Candidates for CO_2 sequestration. Proceedings of the First National Conference on Carbon Sequestration, 14–17.

Alonso-Zarza, A. M., Sánchez-Moya, Y., Bustillo, M. A., Sopen, A., & Delgado, A. (2002). Silicification and dolomitization of anhydrite nodules in argillaceous terrestrial deposits: An example of meteoric-dominated diagenesis from the Triassic of central Spain. *Sedimentology*, *49*(2), 303–317. https://doi.org/10.1046/j.1365-3091.2002.00442.x

Amrani, A., Zhang, T., Ma, Q., Ellis, G. S., & Tang, Y. (2008). The role of labile sulfur compounds in thermochemical sulfate reduction. *Geochimica et Cosmochimica Acta*, *72*(12), 2960–2972. https://doi.org/10.1016/j.gca.2008.03.022

Anderson, G. M., & Thom, J. (2008). The role of thermochemical sulfate reduction in the origin of Mississippi Valley-type deposits: II. Carbonate–sulfide relationships. *Geofluids*, *8*(1), 27–34.

Antler, G., Turchyn, A. V., Rennie, V., Herut, B., & Sivan, O. (2013). Coupled sulfur and oxygen isotope insight into bacterial sulfate reduction in the natural environment. *Geochimica et Cosmochimica Acta*, *118*, 98–117. https://doi.org/10.1016/j.gca.2013.05.005

Banks, D. A., Yardley, B. W. D., Campbell, A. R., & Jarvis, K. E. (1994). REE composition of an aqueous magmatic fluid: A fluid inclusion study from the Capitan Pluton, New Mexico, U.S.A. *Chemical Geology*, *113*(3–4), 259–272. https://doi.org/10.1016/0009-2541(94)90070-1

Banner, J. L., Hanson, G. N., & Meyers, W. J. (1988). Rare earth element and Nd isotopic variations in regionally extensive dolomites from the Burlington-Keokuk Formation (Mississippian): Implications for REE mobility during carbonate diagenesis. *Journal of Sedimentary Research*, *58*(3), 415–432.

Bau, M. (1991). Rare-earth element mobility during hydrothermal and metamorphic fluid-rock interaction and the significance of the oxidation state of europium. *Chemical Geology*, *93*(3-4), 219–230. https://doi.org/10.1016/0009-2541(91)90115-8

Bau, M. (1996). Controls on the fractionation of isovalent trace elements in magmatic and aqueous systems: Evidence from Y/Ho, Zr/Hf, and lanthanide tetrad effect. *Contributions to Mineralogy and Petrology*, *123*(3), 323–333. https://doi.org/10.1007/s004100050159

Bau, M., Balan, S., Schmidt, K., & Koschinsky, A. (2010). Rare earth elements in mussel shells of the Mytilidae family as tracers for hidden and fossil high-temperature hydrothermal systems. *Earth and Planetary Science Letters*, *299*(3-4), 310–316. https://doi.org/10.1016/j.epsl.2010.09.011

Bau, M., & Dulski, P. (1995). Comparative study of yttrium and rare-earth element behaviours in fluorine-rich hydrothermal fluids. *Contributions to Mineralogy and Petrology*, *119*(2-3), 213–223. https://doi.org/10.1007/BF00307282

Bau, M., & Dulski, P. (1996). Distribution of yttrium and rare-earth elements in the Penge and Kuruman iron-formations, Transvaal Supergroup, South Africa. *Precambrian Research*, *79*(1-2), 37–55. https://doi.org/10.1016/0301-9268(95)00087-9

Bau, M., & Dulski, P. (1999). Comparing yttrium and rare earths in hydrothermal fluids from the Mid-Atlantic Ridge: Implications for Y and REE behaviour during near-vent mixing and for the Y/Ho ratio of Proterozoic seawater. *Chemical Geology*, *155*(1-2), 77–90. https://doi.org/10.1016/S0009-2541(98)00142-9

Bau, M., & Möller, P. (1992). Rare earth element fractionation in metamorphogenic hydrothermal calcite, magnesite and siderite. *Mineralogy and Petrology*, *45*(3–4), 231–246. https://doi.org/10.1007/BF01163114

Becker, T. P., & Lynds, R. (2012). A geologic deconstruction of one of the world's largest natural accumulations of CO_2, Moxa arch, southwestern Wyoming. *AAPG Bulletin*, *96*(9), 1643–1664. https://doi.org/10.1306/01251211089

Bickle, M., Kampman, N., & Wigley, M. (2013). Natural analogues. In D. J. DePaolo et al. (Eds.), *Geochemistry of geologic CO_2 sequestration: Reviews in mineralogy and geochemistry* (Vol. 77, pp. 15–71). https://doi.org/10.2138/rmg.2013.77.2

Biehl, B. C., Reuning, L., Schoenherr, J., Lüders, V., & Kukla, P. A. (2016). Impacts of hydrothermal dolomitization and thermochemical sulfate reduction on secondary porosity creation in deeply buried carbonates: A case study from the Lower Saxony Basin, northwest Germany. *AAPG Bulletin*, *100*(4), 597–621. https://doi.org/10.1306/01141615055

Bildstein, O., Worden, R. H., & Brosse, E. (2001). Assessment of anhydrite dissolution as the rate-limiting step during thermochemical sulfate reduction. *Chemical Geology*, *176*(1–4), 173–189. https://doi.org/10.1016/S0009-2541(00)00398-3

Blackstone, D. L. (1979). Geometry of the Prospect-Darby and La Barge faults at their junction with the La Barge platform, Lincoln and Sublette Counties, Wyoming. Geological Survey of Wyoming.

Blondes, M. S., Gans, K. D., Thordsen, J. J., Reidy, M. E., Thomas, B., Engle, M. A., et al. (2014). U.S. Geological Survey National Produced Waters Geochemical Database v2.1 (PROVISIONAL). Energy Resources Program - Produced Waters, 1. Retrieved from http://semanticommunity.info/@api/deki/files/35790/USGS_Produced_Waters_Database_v2.1_Documentation.pdf

Bodnar, R. J. (1993). Revised equation and table for determining the freezing point depression of H2O-Nacl solutions. *Geochimica et Cosmochimica Acta*, *57*(3), 683–684. https://doi.org/10.1016/0016-7037(93)90378-A

Böttcher, M. E., Oelschläger, B., Höpner, T., Brumsack, H. J., & Rullkötter, J. (1998). Sulfate reduction related to the early diagenetic degradation of organic matter and "black spot" formation in tidal sandflats of the German Wadden Sea (southern North Sea): Stable isotope (^{13}C, ^{34}S, ^{18}O) and other geochemical results. *Organic Geochemistry*, *29*(5-7), 1517–1530. https://doi.org/10.1016/S0146-6380(98)00124-7

Budai, C., & Cummings, M. (1987). A depositional model of the Antelope Coal Field, Powder River Basin, Wyoming. *Journal of Sedimentary Petrology*, *57*(1), 30–38. https://doi.org/10.1306/212F8A94-2B24-11D7-8648000102C1865D

Budai, J. (1985). Evidence for rapid fluid migration during deformation, Madison Group, Wyoming and Utah Overthrust Belt. Rocky Mountain Carbonate Reservoirs — A Core Workshop [Golden, CO, August 10–11, 1985], 377–407. Retrieved from http://archives.datapages.com/data/sepm_sp/cw7/Evidence_of_Rapid_Fluid_Migration_during.pdf

Budai, J., Lohmann, K. C., & Owen, R. M. (1984). Burial dedolomite in the Mississippian Madison Limestone, Wyoming and Utah thrust belt. *Journal of Sedimentary Petrology*, *54*(1), 276–288. https://doi.org/10.1306/212F83FF-2B24-11D7-8648000102C1865D

Buoniconti, M. R. (2008). The evolution of the carbonate shelf margins and fill of the Antler Foreland Basin by prograding Mississippian carbonates, northern US Rockies. Open access dissertations. Retrieved from http://scholarlyrepository.miami.edu/oa_dissertations/330

Burdett, J. W., Arthur, M. A., & Richardson, M. (1989). A Neogene seawater sulfur isotope age curve from calcareous pelagic microfossils. *Earth and Planetary Science Letters*, *94*(3-4), 189–198. https://doi.org/10.1016/0012-821X(89)90138-6

Cai, C., Amrani, A., Worden, R. H., Xiao, Q., Wang, T., Gvirtzman, Z., et al. (2016). Sulfur isotopic compositions of individual organosulfur compounds and their genetic links in the lower Paleozoic petroleum pools of the Tarim Basin, NW China. *Geochimica et Cosmochimica Acta*, *182*, 88–108. https://doi.org/10.1016/j.gca.2016.02.036

Cai, C., Hu, W., & Worden, R. H. (2001). Thermochemical sulphate reduction in Cambro–Ordovician carbonates in Central Tarim. *Marine and Petroleum Geology*, *18*(6), 729–741. https://doi.org/10.1016/S0264-8172(01)00028-9

Cai, C., Li, K., Zhu, Y., Xiang, L., Jiang, L., Cai, X., & Cai, L. (2010). TSR origin of sulfur in Permian and Triassic reservoir bitumen, East Sichuan Basin, China. *Organic Geochemistry*, *41*(9), 871–878. https://doi.org/10.1016/j.orggeochem.2010.03.009

Cai, C., Worden, R. H., Bottrell, S. H., Wang, L., & Yang, C. (2003). Thermochemical sulphate reduction and the generation of hydrogen sulphide and thiols (mercaptans) in Triassic carbonate reservoirs from the Sichuan Basin, China. *Chemical Geology*, *202*(1–2), 39–57. https://doi.org/10.1016/S0009-2541(03)00209-2

Cai, C., Xie, Z., Worden, R. H., Hu, G., Wang, L., & He, H. (2004). Methane-dominated thermochemical sulphate reduction in the Triassic Feixianguan Formation East Sichuan Basin, China: Towards prediction of fatal H2S concentrations. *Marine and Petroleum Geology*, *21*(10), 1265–1279. https://doi.org/10.1016/j.marpetgeo.2004.09.003

Cai, C., Zhang, C., Cai, L., Wu, G., Jiang, L., Xu, Z., et al. (2009). Origins of Palaeozoic oils in the Tarim Basin: Evidence from sulfur isotopes and biomarkers. *Chemical Geology*, *268*(3-4), 197–210. https://doi.org/10.1016/j.chemgeo.2009.08.012

Cai, C., Zhang, C., He, H., & Tang, Y. (2013). Carbon isotope fractionation during methane-dominated TSR in East Sichuan Basin gasfields, China: A review. *Marine and Petroleum Geology*, *48*, 100–110. https://doi.org/10.1016/j.marpetgeo.2013.08.006

Came, R. E., Eiler, J. M., Veizer, J., Azmy, K., Brand, U., & Weidman, C. R. (2007). Coupling of surface temperatures and atmospheric CO_2 concentrations during the Palaeozoic era. *Nature*, *449*(7159), 198–201. https://doi.org/10.1038/nature06085

Campbell-Stone, E., Lynds, R., Frost, C., Becker, T. P., & Diem, B. (2011). The Wyoming carbon underground storage project: Geologic characterization of the Moxa Arch and Rock Springs Uplift. *Energy Procedia*, *4*, 4656–4663. https://doi.org/10.1016/j.egypro.2011.02.426

Clark, I. D., & Fritz, P. (1997). *Environmental isotopes in hydrogeology*. New York: CRC Press.

Claypool, G. E., Holser, W. T., Kaplan, I. R., Sakai, H., & Zak, I. (1980). The age curves of sulfur and oxygen isotopes in marine sulfate and their mutual interpretation. *Chemical Geology*, *28*, 199–260. https://doi.org/10.1016/0009-2541(80)90047-9

Claypool, G. E., & Mancini, E. A. (1989). Geochemical relationships of petroleum in Mesozoic reservoirs to carbonate source rocks of Jurassic Smackover Formation, southwestern Alabama. *AAPG Bulletin*, *73*(7), 904–924.

Clayton, R. N., & Mayeda, T. K. (1963). The use of bromine pentafluoride in the extraction of oxygen from oxides and silicates for isotopic analysis. *Geochimica et Cosmochimica Acta*, *27*(1), 43–52. https://doi.org/10.1016/0016-7037(63)90071-1

Clayton, R. N., O'Neil, J. R., & Mayeda, T. K. (1972). Oxygen isotope exchange between quartz and water. *Journal of Geophysical Research*, *77*(17), 3057–3067. https://doi.org/10.1029/JB077i017p03057

Cook, D. J., Randazzo, A. F., & Sprinkle, C. L. (1985). Authigenic fluorite in dolomitic rocks of the Floridan aquifer. *Geology*, *13*(6), 390–391. https://doi.org/10.1130/0091-7613(1985)13<390:AFIDRO>2.0.CO;2

Cross, M. M., Manning, D. A. C., Bottrell, S. H., & Worden, R. H. (2004). Thermochemical sulphate reduction (TSR): Experimental determination of reaction kinetics and implications of the observed reaction rates for petroleum reservoirs. *Organic Geochemistry*, *35*(4), 393–404. https://doi.org/10.1016/j.orggeochem.2004.01.005

De Bruin, R. H. (1991). Wyoming's carbon dioxide resources. *Open File Report, 91–6*, 1–19.

De Bruin, R. H. (2001). Carbon dioxide in Wyoming, information pamphlet 8: Wyoming Geological Survey. Laramie, Wyoming, 1–11.

De Groot, P. A. (2009). *Handbook of stable isotope analytical techniques* (Vol. 2). Amsterdam: Elsevier.

Ding, K., Li, S., & Yue, C. (2009). Simulation experiments on thermochemical origin of high H2S in natural gas. *Energy Sources, Part A: Recovery, Utilization, and Environmental Effects*, *32*(3), 246–255. https://doi.org/10.1080/15567030802092668

Ding, K., Li, S., Yue, C., & Zhong, N. (2008). Simulation experiments on the reaction system of CH_4–$MgSO_4$–H_2O. *Chinese Science Bulletin*, *53*, 1071–1078.

Dixon, J. S. (1982). Regional structural synthesis, Wyoming salient of western overthrust belt. *American Association of Petroleum Geologists Bulletin*, *66*(10), 1560–1580. https://doi.org/10.1306/03B5A98A-16D1-11D7-8645000102C1865D

Dulski, P. (1994). Interferences of oxide, hydroxide and chloride analyte species in the determination of rare earth elements in geological samples by inductively coupled plasma-mass spectrometry. *Fresenius' Journal of Analytical Chemistry*, *350*(4-5), 194–203. https://doi.org/10.1007/bf00322470

Fritz, P., Basharmal, G. M., Drimmie, R. J., Ibsen, J., & Qureshi, R. M. (1989). Oxygen isotope exchange between sulphate and water during bacterial reduction of sulphate. *Chemical Geology: Isotope Geoscience Section*, *79*(2), 99–105. https://doi.org/10.1016/0168-9622(89)90012-2

Frost, C. (2011). Carbon sequestration monitoring activities. UNT Digital Library. Retrieved from http://digital.library.unt.edu/ark:/67531/metadc836030/

Glezakou, V.-A., McGrail, B. P., & Schaef, H. T. (2012). Molecular interactions of SO_2 with carbonate minerals under co-sequestration conditions: A combined experimental and theoretical study. *Geochimica et Cosmochimica Acta*, *92*, 265–274. https://doi.org/10.1016/j.gca.2012.06.015

Goldhaber, M., & Orr, W. (1995). Kinetic controls on thermochemical sulfate reduction as a source of sedimentary H2S. *ACS Symposium Series*, *612*, 412–425. https://doi.org/10.1021/bk-1995-0612.ch023

Goldstein, R. H., & Reynolds, T. J. (1994). Systematics of fluid inclusions in diagenetic minerals: SEPM Short Course 31. *Society for Sedimentary Geology*, *199*.

Gutschick, R. C., & Sandberg, C. A. (1983). Mississippian continental margins of the conterminous United States. The Shelfbreak: Critical Interface on Continental Margins, 79–96. Retrieved from https://www.scopus.com/inward/record.uri?eid=2-s2.0-0021061102&partnerID=40&md5=3c4fb6fb8ea09e723d912cca2217811c

Hao, F., Zhang, X., Wang, C., Li, P., Guo, T., Zou, H., et al. (2015). The fate of CO_2 derived from thermochemical sulfate reduction (TSR) and effect of TSR on carbonate porosity and permeability, Sichuan Basin, China. *Earth-Science Reviews*, *141*, 154–177. https://doi.org/10.1016/j.earscirev.2014.12.001

Hecht, L., Freiberger, R., Gilg, H. A., Grundmann, G., & Kostitsyn, Y. A. (1999). Rare earth element and isotope (C, O, Sr) characteristics of hydrothermal carbonates: Genetic implications for dolomite-hosted talc mineralization at Göpfersgrün (Fichtelgebirge, Germany). *Chemical Geology*, *155*(1-2), 115–130. https://doi.org/10.1016/S0009-2541(98)00144-2

Hesse, R. (1989). Silica diagenesis: Origin of inorganic and replacement cherts. *Earth Science Reviews*, *26*(1-3), 253–284. https://doi.org/10.1016/0012-8252(89)90024-X

Heydari, E., & Moore, C. H. (1989). Burial diagenesis and thermochemical sulfate reduction, Smackover Formation, southeastern Mississippi salt basin. *Geology*, *17*(12), 1080–1084. https://doi.org/10.1130/0091-7613(1989)017<1080:BDATSR>2.3.CO;2

Huang, N. S., Aho, G. E., Baker, B. H., Matthews, T. R., & Pottorf, R. J. (2007). Integrated reservoir modeling to maximize the value of a large sour-gas field with high concentrations of inerts: International Petroleum Technology Conference Paper 11202. IPTC conference in Dubai, UAE.

Jarvis, K. E., Gray, A. L., & McCurdy, E. (1989). Avoidance of spectral interference on europium in inductively coupled plasma mass-spectrometry by sensitive measurement of the doubly charged ion. *Journal of Analytical Atomic Spectrometry*, *4*(8), 743–747. https://doi.org/10.1039/ja9890400743

Jenden, P. D., Titley, P. A., & Worden, R. H. (2015). Enrichment of nitrogen and ^{13}C of methane in natural gases from the Khuff Formation, Saudi Arabia, caused by thermochemical sulfate reduction. *Organic Geochemistry*, *82*, 54–68. https://doi.org/10.1016/j.orggeochem.2015.02.008

Jiang, L., Cai, C., Worden, R. H., Li, K., Xiang, L., Chu, X., et al. (2015). Rare earth element and yttrium (REY) geochemistry in carbonate reservoirs during deep burial diagenesis: Implications for REY mobility during thermochemical sulfate reduction. *Chemical Geology*, *415*, 87–101. https://doi.org/10.1016/j.chemgeo.2015.09.010

Jiang, L., Worden, R. H., & Cai, C. F. (2014). Thermochemical sulfate reduction and fluid evolution of the Lower Triassic Feixianguan Formation sour gas reservoirs, northeast Sichuan Basin, China. *AAPG Bulletin*, *98*(5), 947–973. https://doi.org/10.1306/10171312220

Jochum, K. P., Seufert, H. M., Spettel, B., & Palme, H. (1986). The solar-system abundances of Nb, Ta, and Y, and the relative abundances of refractory lithophile elements in differentiated planetary bodies. *Geochimica et Cosmochimica Acta*, *50*(6), 1173–1183. https://doi.org/10.1016/0016-7037(86)90400-X

Johnson, E. A. (2005). Geologic assessment of undiscovered oil and gas resources in the Phosphoria Total Petroleum System, southwestern Wyoming province, Wyoming, Colorado, and Utah. US Geological Survey Southwestern Wyoming Province Assessment Team, Eds., Petroleum Systems and Geologic Assessment of Oil and Gas in the Southwestern Wyoming Province, Wyoming, Colorado, and Utah: US Geological Survey Digital Data Series DDS-69-D.

Kampschulte, A., Bruckschen, P., & Strauss, H. (2001). The sulphur isotopic composition of trace sulphates in Carboniferous brachiopods: Implications for coeval seawater, correlation with other geochemical cycles and isotope stratigraphy. *Chemical Geology*, *175*(1-2), 149–173. https://doi.org/10.1016/S0009-2541(00)00367-3

Kampschulte, A., & Strauss, H. (2004). The sulfur isotopic evolution of Phanerozoic seawater based on the analysis of structurally substituted sulfate in carbonates. *Chemical Geology*, *204*(3–4), 255–286. https://doi.org/10.1016/j.chemgeo.2003.11.013

Kaszuba, J. P., Navarre-Sitchler, A., Thyne, G., Chopping, C., & Meuzelaar, T. (2011). Supercritical carbon dioxide and sulfur in the Madison LIMESTONE: A natural analog in southwest Wyoming for geologic carbon–sulfur co-sequestration. *Earth and Planetary Science Letters*, *309*(1–2), 131–140. https://doi.org/10.1016/j.epsl.2011.06.033

Katz, D. A. (2008). Early and late diagenetic processes of Mississippian carbonates, northern U. S. Rockies. Open Access Dissertations, Paper 154. Retrieved from http://scholarlyrepository.miami.edu/oa_dissertations/154/

Katz, D. A., Buoniconti, M. R., Montañez, I. P., Swart, P. K., Eberli, G. P., & Smith, L. B. (2007). Timing and local perturbations to the carbon pool in the lower Mississippian Madison Limestone, Montana and Wyoming. *Palaeogeography, Palaeoclimatology, Palaeoecology*, *256*(3-4), 231–253. https://doi.org/10.1016/j.palaeo.2007.02.048

Katz, D. A., Eberli, G. P., Swart, P. K., & Smith, L. B. (2006). Tectonic-hydrothermal brecciation associated with calcite precipitation and permeability destruction in Mississippian carbonate reservoirs, Montana and Wyoming. *AAPG Bulletin*, *90*(11), 1803–1841. https://doi.org/10.1306/03200605072

Kelemen, S. R., Walters, C. C., Kwiatek, P. J., Freund, H., Afeworki, M., Sansone, M., et al. (2010). Characterization of solid bitumens originating from thermal chemical alteration and thermochemical sulfate reduction. *Geochimica et Cosmochimica Acta*, *74*(18), 5305–5332. https://doi.org/10.1016/j.gca.2010.06.013

Kendall, A. C. (2001). Late diagenetic calcitization of anhydrite from the Mississippian of Saskatchewan, western Canada. *Sedimentology*, *48*(1), 29–55. https://doi.org/10.1111/j.1365-3091.2001.00350.x

Kim, S.-T., & O'Neil, J. R. (1997). Equilibrium and nonequilibrium oxygen isotope effects in synthetic carbonates. *Geochimica et Cosmochimica Acta*, *61*(16), 3461–3475. https://doi.org/10.1016/S0016-7037(97)00169-5

King, H. E., Walters, C. C., Horn, W. C., Zimmer, M., Heines, M. M., Lamberti, W. A., et al. (2014). Sulfur isotope analysis of bitumen and pyrite associated with thermal sulfate reduction in reservoir carbonates at the Big Piney–La Barge production complex. *Geochimica et Cosmochimica Acta*, *134*, 210–220. https://doi.org/10.1016/j.gca.2013.11.005

Kiyosu, Y. (1980). Chemical reduction and sulfur-isotope effects of sulfate by organic matter under hydrothermal conditions. *Chemical Geology*, *30*(1–2), 47–56. https://doi.org/10.1016/0009-2541(80)90115-1

Kiyosu, Y., & Krouse, H. R. (1993). Thermochemical reduction and sulfur isotopic behavior of sulfate by acetic acid in the presence of native sulfur. *Geochemical Journal*, *27*(1), 49–57. https://doi.org/10.2343/geochemj.27.49

Kiyosu, Y., & Krouse, R. H. (1990). The role of organic and acid the in the sulfur abiogenic isotope reduction effect. *Geochemical Journal*, *24*(1), 21–27. https://doi.org/10.2343/geochemj.24.21

Knauss, K. G., Johnson, J. W., & Steefel, C. I. (2005). Evaluation of the impact of CO_2, CO-contaminant gas, aqueous fluid and reservoir rock interactions on the geologic sequestration of CO_2. *Chemical Geology*, *217*(3–4), 339–350. https://doi.org/10.1016/j.chemgeo.2004.12.017

Kraig, D. H., Wiltschko, D. V., & Spang, J. H. (1987). Interaction of basement uplift and thin-skinned thrusting, Moxa arch and the Western Overthrust Belt, Wyoming: A hypothesis. *Geological Society of America Bulletin*, *99*(5), 654. https://doi.org/10.1130/0016-7606(1987)99<654:IOBUAT>2.0.CO;2

Leng, M., Barnker, P., Greenwood, P., Roberts, N., & Reed, J. (2001). Oxygen isotope analysis of diatom silica and authigenic calcite from Lake Pinarbasi, Turkey. *Journal of Paleolimnology*, *25*(3), 343–349. https://doi.org/10.1023/a:1011169832093

Leng, M. J., & Sloane, H. J. (2008). Combined oxygen and silicon isotope analysis of biogenic silica. *Journal of Quaternary Science*, *23*(4), 313–319. https://doi.org/10.1002/jqs.1177

Liu, Q. Y., Worden, R. H., Jin, Z. J., Liu, W. H., Li, J., Gao, B., et al. (2013). TSR versus non-TSR processes and their impact on gas geochemistry and carbon stable isotopes in Carboniferous, Permian and Lower Triassic marine carbonate gas reservoirs in the Eastern Sichuan Basin, China. *Geochimica et Cosmochimica Acta*, *100*, 96–115. https://doi.org/10.1016/j.gca.2012.09.039

Liu, Q. Y., Worden, R. H., Jin, Z. J., Liu, W. H., Li, J., Gao, B., et al. (2014). Thermochemical sulphate reduction (TSR) versus maturation and their effects on hydrogen stable isotopes of very dry alkane gases. *Geochimica et Cosmochimica Acta*, *137*, 208–220. https://doi.org/10.1016/j.gca.2014.03.013

Llyod, R. M. (1967). Oxygen-18 composition of oceanic sulfate. *Science (New York, N.Y.)*, *156*(3779), 1228–1231. https://doi.org/10.1126/science.156.3779.1228

Lüders, V., Möller, P., & Dulski, P. (1993). REE fractionation in carbonates and fluorite. *Monograph Series on Mineral Deposits*, *30*(9), 133–150.

Lynds, R., Campbell-Stone, E., Becker, T. P., & Frost, C. D. (2010). Stratigraphic evaluation of reservoir and seal in a natural CO_2 field: Lower Paleozoic, Moxa Arch, southwest Wyoming. *Rocky Mountain Geology*, *45*(2), 113–132. https://doi.org/10.2113/gsrocky.45.2.113

Machel, H. G. (1987a). Saddle dolomite as a by-product of chemical compaction and thermochemical sulfate reduction. *Geology*, *15*(10), 936–940. https://doi.org/10.1130/0091-7613(1987)15<936:SDAABO>2.0.CO;2

Machel, H. G. (1987b). Some aspects of diagenetic sulphate-hydrocarbon redox reactions. *Geological Society, London, Special Publications*, *36*(1), 15–28. https://doi.org/10.1144/GSL.SP.1987.036.01.03

Machel, H. G. (2001). Bacterial and thermochemical sulfate reduction in diagenetic settings—Old and new insights. *Sedimentary Geology*, *140*(1-2), 143–175. https://doi.org/10.1016/S0037-0738(00)00176-7

Machel, H. G., Krouse, H. R., & Sassen, R. (1995). Products and distinguishing criteria of bacterial and thermochemical sulfate reduction. *Applied Geochemistry*, *10*(4), 373–389. https://doi.org/10.1016/0883-2927(95)00008-8

Marenco, P. J., Corsetti, F. A., Hammond, D. E., Kaufman, A. J., & Bottjer, D. J. (2008). Oxidation of pyrite during extraction of carbonate associated sulfate. *Chemical Geology*, *247*(1–2), 124–132. https://doi.org/10.1016/j.chemgeo.2007.10.006

McLennan, S. M. (1989). Rare earth elements in sedimentary rocks: Influence of provenance and sedimentary processes. *Reviews in Mineralogy and Geochemistry*, *21*(1), 169–200.

Merrill, M. D., Hunt, A. G., & Lohr, C. D. (2014). Noble gas geochemistry investigation of high CO_2 natural gas at the LaBarge Platform, Wyoming, USA. *Energy Procedia*, *63*, 4186–4190. https://doi.org/10.1016/j.egypro.2014.11.451

Meshoulam, A., Ellis, G. S., Said Ahmad, W., Deev, A., Sessions, A. L., Tang, Y., et al. (2016). Study of thermochemical sulfate reduction mechanism using compound specific sulfur isotope analysis. *Geochimica et Cosmochimica Acta*, *188*, 73–92. https://doi.org/10.1016/j.gca.2016.05.026

Michard, A. (1989). Rare earth element systematics in hydrothermal fluids. *Geochimica et Cosmochimica Acta*, *53*(3), 745–750. https://doi.org/10.1016/0016-7037(89)90017-3

Middleton, G. V. (1961). Evaporite solution breccias from the Mississippian of Southwest Montana. *Journal of Sedimentary Petrology*, *31*(2), 189–195. https://doi.org/10.1306/74D70B32-2B21-11D7-8648000102C1865D

Milliken, K. L. (1979). The silicified evaporite syndrome—Two aspects of silicification history of former evaporite nodules from southern Kentucky and northern Tenessee. *Journal of Sedimentary Petrology*, *49*(1), 245–256. https://doi.org/10.1306/212F7707-2B24-11D7-8648000102C1865D

Mitra, A., Elderfield, H., & Greaves, M. J. (1994). Rare earth elements in submarine hydrothermal fluids and plumes from the Mid-Atlantic Ridge. *Marine Chemistry*, *46*(3), 217–235. https://doi.org/10.1016/0304-4203(94)90079-5

Möller, P. (1983). Lanthanoids as a geochemical probe and problems in lanthanoid geochemistry distribution and behaviour of lanthanoids in non-magmatic-phases. In S. P. Sinha (Ed.), *Systematics and the properties of the lanthanides* (pp. 561–616). Dordrecht, Netherlands: Springer. https://doi.org/10.1007/978-94-009-7175-2_13

Möller, P. (1997). Rare earth element and yttrium fractionation caused by fluid migration. *Journal of Geosciences*, *42*(3), 43.

Möller, P., Dulski, P., Savascin, Y., & Conrad, M. (2004). Rare earth elements, yttrium and Pb isotope ratios in thermal spring and well waters of West Anatolia, Turkey: A hydrochemical study of their origin. *Chemical Geology*, *206*(1–2), 97–118. https://doi.org/10.1016/j.chemgeo.2004.01.009

Möller, P., Stober, I., & Dulski, P. (1997). Seltenerdelement-, Yttrium-Gehalte und Bleiisotope in Thermal- und Mineralw {ä} ssern des Schwarzwaldes. *Grundwasser*, *2*(3), 118–132. https://doi.org/10.1007/s767-1997-8533-0

Moore, C. H. (1995). Gas production from a super-deep dolomite reservoir, Madden field, Wind River basin, Wyoming, U.S.A. American Association of Petroleum Geologists Hedberg Conference, "Carbonate Reservoirs of the World: Problems, solutions and strategies for the future," Pau, France, session 3, paper 17.

Moore, C. H. (2001). Carbonate reservoirs: Porosity evolution and diagenesis in a sequence stratigraphic framework. *Developments in sedimentology* (Vol. 55, p. 444). Amsterdam: Elsevier.

Nance, W. B., & Taylor, S. R. (1976). Rare earth element patterns and crustal evolution—I. Australian post-Archean sedimentary rocks. *Geochimica et Cosmochimica Acta*, *40*(12), 1539–1551. https://doi.org/10.1016/0016-7037(76)90093-4

Newton, R. J., Pevitt, E. L., Wignall, P. B., & Bottrell, S. H. (2004). Large shifts in the isotopic composition of seawater sulphate across the Permo–Triassic boundary in northern Italy. *Earth and Planetary Science Letters*, *218*(3-4), 331–345. https://doi.org/10.1016/S0012-821X(03)00676-9

Nozaki, Y., Zhang, J., & Amakawa, H. (1997). The fractionation between Y and Ho in the marine environment. *Earth and Planetary Science Letters*, *148*(1-2), 329–340. https://doi.org/10.1016/S0012-821X(97)00034-4

Ohmoto, H., & Rye, R. O. (1979). Isotopes of sulfur and carbon. In H. L. Barnes (Ed.), *Geochemistry of hydrothermal ore deposits* (pp. 509–567). New York: John Wiley.

Ohr, M., Halliday, A. N., & Peacor, D. R. (1994). Mobility and fractionation of rare earth elements in argillaceous sediments: Implications for dating diagenesis and low-grade metamorphism. *Geochimica et Cosmochimica Acta*, *58*(1), 289–312. https://doi.org/10.1016/0016-7037(94)90465-0

Orr, W. L. (1974). Changes in sulfur content and isotopic ratios of sulfur during petroleum maturation—Study of Big Horn basin Paleozoic oils. *AAPG Bulletin*, *58*(11), 2295–2318.

Pearce, J. K., Golab, A., Dawson, G. K. W., Knuefing, L., Goodwin, C., & Golding, S. D. (2016). Mineralogical controls on porosity and water chemistry during O_2-SO_2-CO_2 reaction of CO_2 storage reservoir and cap-rock core. *Applied Geochemistry*, *75*, 152–168. https://doi.org/10.1016/j.apgeochem.2016.11.002

Piqué, À., Canals, À., Disnar, J. R., & Grandia, F. (2009). In situ thermochemical sulfate reduction during ore formation at the Itxaspe Zn-(Pb) MVT occurrence (Basque-Cantabrian basin, Northern Spain). *Geologica Acta*, *7*(4), 431–449. https://doi.org/10.1344/105.000001448

Powell, T. G., & MacQueen, R. W. (1984). Precipitation of sulfide ores and organic matter: Sulfate reactions at Pine Point, Canada. *Science*, *224*(4644), 63–66. https://doi.org/10.1126/science.224.4644.63

Riciputi, L. E. E. R., Macheu, H. G., & Colp, D. R. (1994). An ion microprobe study of diagenetic carbonates in the Devonian Nisku Formation of Alberta, Canada. *Geochimica et Cosmochimica Acta*, *1*, 115–127.

Roberts, A. E. (1966). Stratigraphy of the Madison Group near Livingston, Montana and discussion of karst and solution-breccia features. U. S. Geological Survey Professional Paper, (526–B), B1–B23. techreport.

Roberts, L. N. R., Lewan, M. D., & Finn, T. M. (2005). Burial history, thermal maturity, and oil and gas generation history of petroleum systems in the southwestern Wyoming province, Wyoming, Colorado and Utah. US Geological Survey Southwest Wyoming Province Assessment Team: Petroleum Systems and Geologic Assessment of Oil and Gas in the Southwestern Wyoming Province, Wyoming, Colorado, and Utah: US Geological Survey Digital Data Series DDS-69-D.

Robinson, B. W., & Kusakabe, M. (1975). Quantitative preparation of sulfur dioxide, for sulfur-34/sulfur-32 analyses, from sulfides by combustion with cuprous oxide. *Analytical Chemistry*, *47*(7), 1179–1181. https://doi.org/10.1021/ac60357a026

Romanek, C. S., Grossman, E. L., & Morse, J. W. (1992). Carbon isotopic fractionation in syntetic aragonite and calcite: Effects of temperature and precipitation rate. *Geochimica et Cosmochimica Acta*, *56*(1), 419–430. https://doi.org/10.1016/0016-7037(92)90142-6

Sando, W. J. (1976). Mississippi history of the northern Rocky Mountains region. *Journal of Research of the U.S. Geological Survey*, *4*(3), 317–338.

Schmidt, K., Koschinsky, A., Garbe-Schönberg, D., de Carvalho, L. M., & Seifert, R. (2007). Geochemistry of hydrothermal fluids from the ultramafic-hosted Logatchev hydrothermal field, 15 N on the Mid-Atlantic Ridge: Temporal and spatial investigation. *Chemical Geology*, *242*(1), 1–21.

Sheppard, S. M. F., & Schwarz, H. P. (1970). Fractionation of carbon and oxygen isotopes and magnesium between coexisting metamorphic calcite and dolomite. *Contributions to Mineralogy and Petrology*, *26*(3), 161–198. https://doi.org/10.1007/BF00373200

Smith, L. B., Eberli, G. P., & Sonnenfeld, M. (2004). Sequence-stratigraphic and paleogeographic distribution of reservoir-quality dolomite, Madison Formation, Wyoming and Montana. *AAPG Memoir*, *85*(80), 67–92. https://doi.org/10.1306/61EED030-173E-11D7-8645000102C1865D

Smith, T. M. (1991). Diagenesis of shallow marine carbonate rocks: Isotopic and trace element constraints from the Mississippian Mission Canyon Formation, central and southwestern Montana. Texas A&M University.

Sonnenfeld, M. (1996a). An integrated sequence stratigraphic approach to reservoir characterization of the Lower Mississippian Madison Limestone, emphasizing Elk Basin Field, Bighorn Basin, Wyoming and Montana. Colorado School of Mines. Retrieved from https://books.google.co.uk/books?id=g4TatwAACAAJ

Sonnenfeld, M. (1996b). Sequence evolution and hierarchy within the lower Mississippian Madison Limestone of Wyoming. Paleozoic Systems of the Rocky MountainThe Region, 165–192. Retrieved from http://archives.datapages.com/data/rocky_sepm/data/034/034001/165_rocky_mount340165.htm

Stilwell, D. P. (1989). CO_2 resources of the Moxa Arch and the Madison Reservoir, 105–115.

Strebel, O., Böttcher, J., & Fritz, P. (1990). Use of isotope fractionation of sulfate-sulfur and sulfate-oxygen to assess bacterial desulfurication in a sandy aquifer. *Journal of Hydrology*, *121*(1–4), 155–172. https://doi.org/10.1016/0022-1694(90)90230-U

Sverjensky, D. A. (1984). Europium redox equilibria in aqueous solution. *Earth and Planetary Science Letters*, *67*(1), 70–78. https://doi.org/10.1016/0012-821X(84)90039-6

Tanaka, K., & Kawabe, I. (2006). REE abundances in ancient seawater inferred from marine limestone and experimental REE partition coefficients between calcite and aqueous solution. *Geochemical Journal*, *40*(5), 425–435. https://doi.org/10.2343/geochemj.40.425

Thayer, P. A. (1983). Relationship of porosity and permeability to petrology of the Madison Limestone in rock cores from three test WeUs in Montana and Wyoming relationship of porosity and permeability to petrology of the Madison Limestone in rock cores from three test wells i. Geological Survey Paper 1273-C.Retrieved from https://pubs.er.usgs.gov/pubs/pp/pp1273C

Veizer, J., Godderis, Y., & François, L. M. (2000). Evidence for decoupling of atmospheric CO_2 and global climate during the Phanerozoic eon. *Nature*, *408*(6813), 698–701. https://doi.org/10.1038/35047044

Wach, P. H. (1977). The Moxa Arch, an overthrust model? Wyoming Geological Association, 29th Annual Field Conference, 651–664.

Wallmann, K. (2004). Impact of atmospheric CO_2 and galactic cosmic radiation on Phanerozoic climate change and the marine $\delta^{18}O$ record. *Geochemistry, Geophysics, Geosystems*, *5*, Q06004. https://doi.org/10.1029/2003GC000683

Williams, R. H., & Paulo, S. (2002). Major roles for fossil fuels in an environmentally constrained world. Sustainability in Energy Production and Utilization in Brazil: The next Twenty Years,2002(February), 18–20. Retrieved from http://www.feagri.unicamp.br/energia/energia2002/jdownloads/pdf/papers/paper_Williams.pdf

Worden, R. H., & Smalgeoley, P. C. (1996). H2S-producing reactions in deep carbonate gas reservoirs: Khuff Formation, Abu Dhabi. *Chemical Geology*, *133*(1-4), 157–171. https://doi.org/10.1016/S0009-2541(96)00074-5

Worden, R. H., Smalley, P. C., & Cross, M. M. (2000). The influence of rock fabric and mineralogy on thermochemical sulfate reduction: Khuff Formation, Abu Dhabi. *Journal of Sedimentary Research*, *70*(5), 1210–1221. https://doi.org/10.1306/110499701210

Worden, R. H., Smalley, P. C., & Oxtoby, N. H. (1995). Gas souring by thermochemical sulfate reduction at 140 C. *AAPG Bulletin*, *79*(6), 854–863.

Wynn, J. G., Sumrall, J. B., & Onac, B. P. (2010). Sulfur isotopic composition and the source of dissolved sulfur species in thermo-mineral springs of the Cerna Valley, Romania. *Chemical Geology*, *271*(1–2), 31–43. https://doi.org/10.1016/j.chemgeo.2009.12.009

Wynn, P. M., Fairchild, I. J., Baker, A., Baldini, J. U. L., & McDermott, F. (2008). Isotopic archives of sulphate in speleothems. *Geochimica et Cosmochimica Acta*, *72*(10), 2465–2477. https://doi.org/10.1016/j.gca.2008.03.002

Wynn, P. M., Loader, N. J., & Fairchild, I. J. (2014). Interrogating trees for isotopic archives of atmospheric sulphur deposition and comparison to speleothem records. *Environmental Pollution*, *187*, 98–105. https://doi.org/10.1016/j.envpol.2013.12.017

Xiao, Y., Xu, T., & Pruess, K. (2009). The effects of gas-fluid-rock interactions on CO_2 injection and storage: Insights from reactive transport modeling. *Energy Procedia*, *1*(1), 1783–1790. https://doi.org/10.1016/j.egypro.2009.01.233

Yue, C., Li, S., Ding, K., & Zhong, N. (2005). Study of simulation experiments on the TSR system and its effect on the natural gas destruction. *Science in China Series D: Earth Sciences*, *48*(8), 1197–1202. https://doi.org/10.1360/03yd0133

Yue, C., Li, S., Ding, K., & Zhong, N. (2006). Thermodynamics and kinetics of reactions between C1—C3 hydrocarbons and calcium sulfate in deep carbonate reservoirs. *Geochemical Journal*, *40*(1), 87–94. https://doi.org/10.2343/geochemj.40.87

Zhang, W., Xu, T., & Li, Y. (2011). Modeling of fate and transport of coinjection of H2S with CO_2 in deep saline formations. *Journal of Geophysical Research*, *116*, B02202. https://doi.org/10.1029/2010JB007652

Zhong, S., & Mucci, A. (1995). Partitioning of rare earth elements (REEs) between calcite and seawater solutions at 25 C and 1 atm, and high dissolved REE concentrations. *Geochimica et Cosmochimica Acta*, *59*(3), 443–453. https://doi.org/10.1016/0016-7037(94)00381-U